Continuous Doping of La_2CuO_{4+x} Thin Films

A THESIS
SUBMITTED TO THE FACULTY OF THE GRADUATE SCHOOL
OF THE UNIVERSITY OF MINNESOTA
BY

Joseph Kinney

IN PARTIAL FULFILLMENT OF THE REQUIREMENTS
FOR THE DEGREE OF
DOCTORATE OF PHILOSOPHY

Allen Goldman

September, 2015

Acknowledgements

There are many many wonderful people in my life who have shown me all kinds of support throughout the process of earning this PhD. My adviser Allen Goldman who was always positive and supportive no matter how stuck or discouraged I got at times. My labmates Javier, Alexi, JJ, Ilana, Terry, Boyi, Joe, Yeonbae, Steve, Yen Hsiang, Xiang Leng, and Yu Chen, who provided guidance and a helping hand throughout this experience. Bharat Jalan and Alex Kamenev who have been helpful sounding boards and were kind enough to serve on my committee. Paul Crowell who knows everything and does everything. I am pretty sure the department would not exist without all of his work. The staff of the machine shop, Peter, Jon, Bill, Ron, George and Roger who shared their expertise whenever I wanted to build something and did not know how. Kurt, who made teaching MXP one of the highlights of my experience here and was always helpful in encouraging me to get away from physics at times and go on an adventure in the boundary waters. The members of my incoming class, Lee, Kate, Elizabeth, Brian, Nick and Abe who have become wonderful friends through out this shared challenge. I know this experience was infinitely more enjoyable as a result of their presence and I am glad to now have them all in my life. Finally, I want to thank my family. My Mom, Dad, brothers, and sister who may have thought I was a little crazy and stubborn for pushing down this path at times but always showed me nothing

but love and support.

This work was primarily supported by the National Science Foundation through the University of Minnnesota MRSEC under Award Number DMR-1420013 and partially supported by the National Science Foundation under Award Number DMR-1209578. Part of this work was carried out at the University of Minnesota Characterization Facility, a member of the NSF-funded Materials Research Facilities Network via the MRSEC program, and the Nanofabrication Center which receives partial support from the NSF through the NNIN program.

Abstract

Finding more efficient ways of exploring the doping phase diagrams of high temperature superconductors as well as probing the fundamental properties of these materials are essential ingredients for driving the discovery of new materials. We use a doping technique involving gating with ionic liquids to systematically and continuously tune the T_c of superconducting La_2CuO_{4+x} thin films. We probe both the transport properties and the penetration depth of these samples and find that Homes scaling $\lambda^{-2} \propto \sigma T_c$ is obeyed, consistent with these materials being in the dirty limit. This result is independent of the precise mechanism for the gating process as all of the parameters of the scaling relationship are determined by direct measurements on the films.

Contents

List of Tables

List of Figures

Chapter 1

Introduction

The field of superconductivity dates back to the initial discovery by Heike Kamerlingh Onnes in Mercury more than 100 years ago. The two fundamental properties that make something a superconductor are zero resistance and the Meissner effect. Zero resistance means the ability to transfer charge without dissipation. The Meissner effect is the expulsion of magnetic fields from inside the superconducting material. We will be interested in both of these properties as we probe the materials presented in this work. The idea of a material having zero resistance presents a number of possible applications. For example, one could build power lines out of superconducting wires and there would be no loss in power no matter how long the lines were. Another example would be to build coils out of superconducting wire and store energy by ramping up a dc current which will flow indefinitely in the superconducting loop. Versions of both of these applications are in use today, but the major drawback with the current materials is they all have superconducting transition temperatures, the temperature below which the materials are superconductors, that are well below room temperature. This means all of these applications require some form of sophisticated cooling in order to make them

work. There are many cases where this cost in cooling is worth the benefit of zero resistance. Every MRI in use today is built using magnets constructed out of superconducting wire. However, there is a strong desire to find materials with higher transition temperatures, ideally greater than room temperature.

This study of high-T_c materials was initiated by the discovery of superconductivity in Lanthanum Barium Copper Oxide (LBCO) 30 years ago [1]. Figure 1.1 shows this discovery in context with the overall evolution of material discovery in the field of superconductivity. LBCO is in a class of materials know as the Cuprates. The common characteristic of all Cuprates is a CuO_2 plane. These layered oxide materials are built from stacks of many different compounds where the layers between the copper oxygen planes often serve as charge reservoirs for adding and removing dopants. We will explore using ionic liquid as an alternative method for adjusting the doping of these materials. The idea is that by using ionic liquids we can change the properties of a material just by applying a gate voltage. This convenience allows us to cover a lot of ground in the doping phase diagram of this materials in an efficient way. Where typically one would need to grow a whole series of samples all at slightly different dopings, we can grow a single sample and continuously tune the doping of that material using ionic liquids. We will see that this pretty picture of turning a knob and cleanly effecting the doping of a sample is an oversimplified one and there will be disorder and structure changes in addition to doping changes that we will need to be aware of and take into account.

There are two basic strategies for finding superconductors with high transition temperatures. The first is to blindly guess and then check and see if that material is a superconductor and what is its transition temperature. While this is clearly not the most systematic of strategies it has largely been the most successful up

until now. An example of this strategy at work was the discovery of a whole new family of materials, similar to the Cuprates in that they are layered compounds, but based on Iron Arsenic layers at their core [2]. Before this discovery conventional wisdom would have said that magnetic materials are a bad choice if one is trying to build a superconductor, and this materials discovery came as quite a surprise. There are a great many details about both the Cu and Fe based superconductors that are not well understood, and there is optimism that one can compare and contrast these two families to hopefully focus in on the essential properties that make these materials superconductors with relatively high transition temperatures. While up until now much of the success in finding better superconductors has been close to a random search, there is optimism that we can better understand the fundamentals of these materials and use that to inform our material search.

The work presented in this thesis approaches the problem of high temperature superconductivity on two fronts. First, we use ionic liquids to more efficiently adjust the doping in these materials. This is an improved version of the guess and check method. Second, we carefully track both the resistance and penetration depth of the material and see that there are fundamental scaling relationships between these quantities. The idea is that by finding these fundamental relationships we can better understand the key ingredients that make up a superconductor and use that information going forward to find better materials.

Before we can get to tuning superconductors using ionic liquids or exploring the fundamentals of these materials, we must first produce superconducting samples. The material we will study in this thesis is La_2CuO_{4+x} (LCO). The transition temperature of this material when optimally doped is slightly above 40K. We produce thin films of this material using ozone assisted Molecular Beam Epitaxy

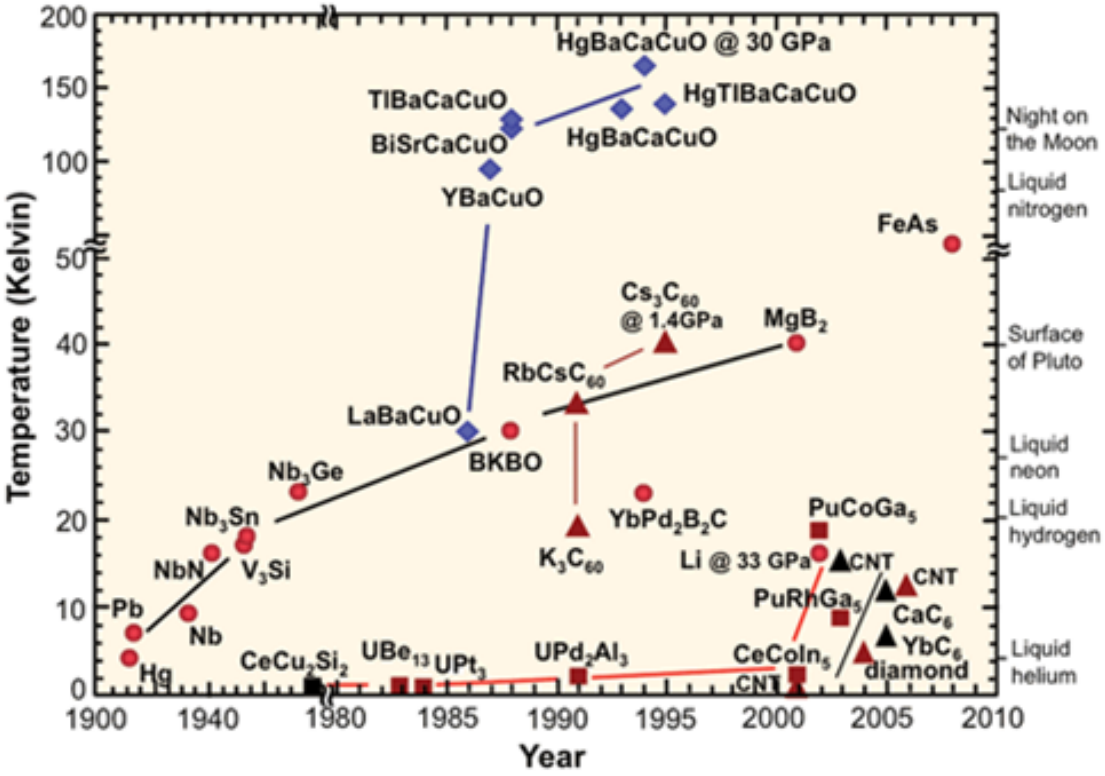

Figure 1.1: Figure taken from[3]. Critical temperature of material plotted against the year in which that material was discovered. The landmark discovery by Bednorz and Muller of LBCO in 1986 sparked a flurry of research activity that continues to today.

(MBE). By thin we mean 3-4 unit cells thick, which is roughly 30-40 nm. This is the minimal thickness we can produce and have a single superconducting transition throughout the entire film. The thin nature of these films make them prime candidates for doping using ionic liquid. Ionic liquid will have a limited depth over which it can affect a material and in the case of these ultra thin materials we can alter the entire thickness of the sample using ionic liquids. Chapter 2 will focus on the material growth techniques used to produce the LCO samples studied in this thesis.

Once we have a high quality LCO sample the next step is to tune this materials properties using ionic liquids. The field of using ionic liquids to adjust the doping of thin films is a relatively new one and there are still many details of the doping process that are not fully understood. The naive picture is that by applying a voltage between a gate electrode and the sample, both of which are immersed in ionic liquid, one can force a buildup of ions on the surface of the sample. This charge layer on the surface of the sample induces charges in the material thereby changing the doping of the material. In reality there are also chemical and structural changes induced by the ionic liquid on the surface of the sample. In fact, just adding ionic liquid to the surface of LCO without applying a gate voltage will increase the normal state resistance of the sample and decrease T_c. We will explore to what extent we can control all of these factors and demonstrate that despite some of these drawbacks, ionic liquids are still a powerful and useful tool for studying high temperature superconductors. Chapter 3 will cover the details of how we use ionic liquids and highlight some of the limitations of this technique.

The next goal of this work is to explore more carefully the fundamental nature of the superconducting state. The focus of this thesis will be on the use of a two-coil mutual inductance technique for probing the penetration depth of the superconducting samples. In parallel with this two-coil measurement we will look at the resistance and Hall Effect as well. Measuring the resistance of a superconductor is informative but only up to a point. In particular, once the sample transitions into the superconducting state, we see that the resistance is zero but cannot say anything move detailed than this. Alternatively, the two-coil measurement, which probes the penetration depth of the material, can quantify the strength of the superconducting state. Not just is the sample superconducting but

just how good a superconductor it is. In particular, there is a direct relationship between the penetration depth and the superconducting electron density. Where measuring zero resistance implies there are some electrons in the superconducting state, measuring the penetration depth allows us to quantify how many electrons are in the superconducting state. Section 4.2 will detail the experimental setup used for making two-coil mutual inductance measurements in conjunction with ionic liquid doping. Also we will walk through the numerical procedure used to invert the measured voltage data to determine the penetration depth of the film.

The final piece of the puzzle will be presented in Chap. 5, where we will put together our measurements of both the transport and penetration depth and explore the fundamental ways in which these quantities are related. This will closely follow previous work[4, 5] where it was shown that $\lambda^{-2} \propto \sigma T_c$, where σ is the conductivity of the material, T_c is the critical temperature, λ is the penetration depth of the sample and λ^{-2} is proportional to the superconducting electron density. The idea is that in a wide variety of superconducting samples there is scaling relationship between T_c and the number of charge carriers above the superconducting transition in the normal state and the number of charge carriers that condense into the superconducting state. We find that our samples follow this same universal scaling, which demonstrates the robustness of this relationship. In particular we are coming to this conclusion using a combination of novel techniques. Both the sample preparation, using thin films and doping with ionic liquids, as well as the measurement probes, standard four-terminal resistance with two coil mutual inductance, are new paths for verifying this conclusion.

The work presented in this thesis addresses both technical challenges as well as fundamental physics. We demonstrate how ionic liquids are a powerful tool for producing large changes in the physical properties of thin film superconducting

samples. This allows one to study the properties of these films in an efficient and systematic way. Where it previously would require a whole series of sample growths we can do the same study in a single sample. This is not just an advantage in terms of time, but also fixes all the geometrical factors in the sample that would otherwise introduce uncertainty in comparing one sample to the next. This thesis presents a systematic study of LCO where we monitor the interplay between the resistance, the penetration depth, and the critical temperature of this material. We see that the previously observed scaling relationship of $\lambda^{-2} \propto \sigma T_c$ extends to LCO samples doped using ionic liquids.

Chapter 2

Material Growth and Characterization

Our goal is to study the underlying physics of superconducting materials. An obvious first step in this process is producing superconducting materials. We will focus on the material La_2CuO_{4+x}, which at optimal doping has a transition temperature of approximate 40 K. We use ozone assisted Molecular Beam Epitaxy (MBE) in order to produce thin films of this material and use a variety of characterization procedures to check the films both during the growth and after the growth. This chapter will walk through the recipe we follow to produce thin films of La_2CuO_{4+x} . In Sec. 2.1 we will detail the procedures used as well as discuss some of the limitations in terms of source stability and how this effects the overall yield of the films that we produce. In order to produce films with high single superconducting transition temperatures throughout the film one must first start with a substrate and Sec. 2.2 covers the characterization of the substrates we use in more detail. In particular, we will show that the films we get from MTI, without any processing, show distinct terrace structure and sharp rocking curves

indicating they are of high quality. Finally, in Sec. 2.3 we will cover the many probes we use to asses the properties of the films both during the growth and after they have been removed from the deposition chamber. All this is the first step in the larger goal of this thesis which is to take these superconducting films and continually tune their doping using ionic liquids and monitor the underlying superconducting properties.

2.1 Molecular Beam Epitaxy

Molecular Beam Epitaxy (MBE) is the tool we use for producing thin films of La_2CuO_{4+x}. MBE is a technique used for very precisely controlling the flux of materials to the point where we can build films one atomic layer at a time. For the growth of La_2CuO_{4+x} we use Knudsen type effusion sources (K-cells) for both lanthanum and copper, and we use a distillation procedure for creating a pure source of ozone gas which reacts with the film. The film is grown on a $SrLaAlO_4$ substrate which is held at high temperatures during the growth. The success of MBE growth depends primarily on the precise control of the flux of the source elements and we will discuss both how this is achieved and to what extent we are limited in this regard. A schematic of the MBE setup used for producing the samples in this study is shown in Fig. 2.1. The copper and lanthanum K-cells are located on the bottom of the chamber and a glass pipe coated in gold delivers ozone to a pair of points on either side of the substrate during the film growth. The ozone pipe is coated in gold to reflect the radiation from the sources and minimize heating. The ozone will dissociate and recombine into O_2 at a rate that increases the warmer the temperature and we want to maximize the concentration of ozone that arrives at our sample. We use a quartz crystal monitor (QCM) to measure

the material flux rate of the lanthanum and copper sources. Both the sample stage and QCM can be moved. Our procedure is prior to the growth, we position the QCM in the location where the substrate will be during growth and measure the rates of lanthanum and copper. This means we do not need an additional tooling factor calibration on these rate measurements. After we have measured the rates we remove the QCM and move the substrate into its place. We then introduce ozone to a pressure of $3x10^{-5}$ Torr and heat the substrate up to 700 °C. This temperature was optimized by growing a series of films at temperatures from 500 °C to 900 °C and measuring the two terminal resistance of each film. For 4 unit cell films, the resistance decreased from 2 kΩto 1 kΩwith increasing temperature up to 750 °C. Above 750 °C the resistance of the films increased sharply to ¿1 MΩ. The flux of material from the K-cells can be selectively blocked by a shutter for each element. We control the amount of material we deposit by opening these shutters for a precise amount of time. For the flux rates we use a typical shutter time of 30 seconds to deposit material in 1/2 unit cell increments. The unit cell of La_2CuO_{4+x} is composed of pair of repeating layers. We deposit in 1/2 unit cell increments, which each contain a complete formula unit. The shutter time is a compromise between two competing goals. The time it takes for the shutter to move from the closed to the open position is about 1 sec. Having the shutter open for 30 seconds means that the uncertainty in the amount of material deposited during the time the shutter is moving is relatively small compared to the overall total amount of material during the time the shutter was open. On the other hand we do not want to choose a time arbitrarily long because there are limits to the stability of the sources and the longer the sample growth the more likely the current material flux rate will deviate from the measured flux rate from before the deposition. After we have deposited the desired amount of material we then

turn off the substrate heater and let the sample slowly cool still in the presence of ozone. Once the sample has reached 50-100 °C we turn off the ozone source and recollect any extra ozone with a sorption pump which vents through a catalyst to fully react the ozone before it is exhausted into the laboratory.

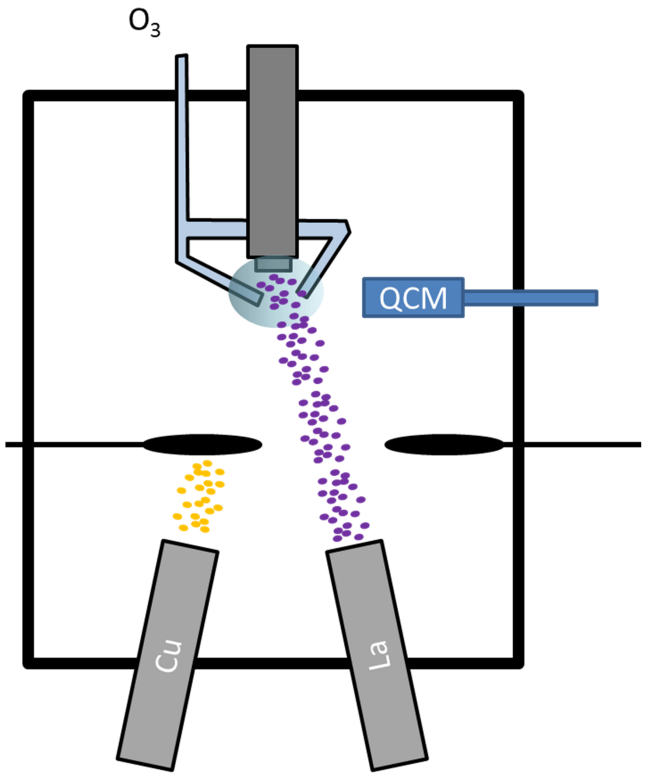

Figure 2.1: Schematic diagram of the MBE used for producing La_2CuO_{4+x} films. We use distilled ozone to ensure sufficient oxygenation of the films and control the amount of La and Cu by timed shutters.

One of our primary concerns for growing high quality samples is precisely controlling the material flux from the lanthanum and copper sources. We use k-cell effusion sources for both materials. Lanthanum has a melting point of 920 °C and after the sources has been warmed up from room temperature we always keep

it above this point. For lanthanum we use an idle temperature of 1000 °C and a deposition temperature of 1500 °C. Copper has a melting point of 1085 °C and like lanthanum we hold the source above this point after the initial warm up. We use an idle temperature of 1100 °C and a deposition temperature of 1200 °C for copper. For both materials the deposition rate measured at the idle temperature is 100 times smaller than the rate measured at the deposition temperature. Both sources are held at their respective temperatures using Micristar controllers. We measure the flux rate of both sources prior to the film growth using a QCM. We are making the assumption that the sources stay stable during the time between when we measure this rate and when we actually deposit the sample. This time delay is approximately one hour. We have done careful studies of the stability over time for the lanthanum and copper sources and this assumption of stability is not confirmed. Ideally the fluctuations in flux rate would be no larger than 1 %. In order to measure the rate to a resolution of 1 % requires monitoring the QCM for 5-10 min. Fig. 2.2 shows an example of where this 5-10 min measurement was repeated several times over the course of a day in order to see the long time stability of the sources. We see that on time scales on the order of hours there are drifts in the flux rate larger than 10 %. This means that we are not actually maintaining the desired stability. The source of this instability is likely linked to temperature fluctuations. We maintain temperature stability of 1 part in 1000, but due to the exponential nature of the deposition rate this can still result in significant changes in the deposition rate. For example, an increase of 10 °C in the temperature of lanthanum K-cell will produce a 50% increase in the deposition rate. As a result of this instability, the variation from one sample growth to the next is very high. The result of this thesis will focus on samples that showed sharp superconducting transitions at a single temperature under the assumption that

these samples were grown where the growth conditions were optimal even though we could not always reproduce these same conditions.

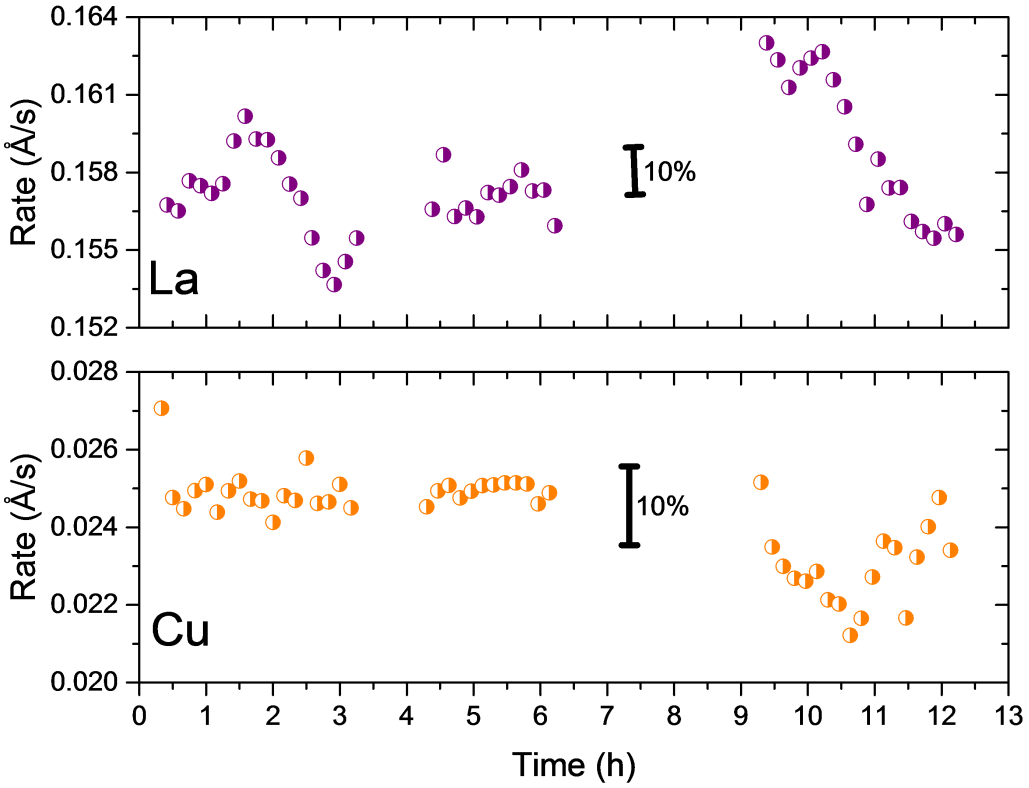

Figure 2.2: Deposition rate stability of the lanthanum and copper sources over the course of half a day. Both rates change over time by more than 10%.

A complication on top of the rate stability issue just outlined is that our measurement of the rate, particularly copper, is sensitive to the cooling water temperature of the QCM. The frequency that the QCM measures is a function of its temperature and changes in this temperature will look like a flux of material. Basically, when we measure the stability of the source we are actually measuring a convoluted stability of both the source and the QCM temperature. Fig. 2.3 shows oscillations in the measured copper flux rate. This measurement was done

with the copper shutter closed, which means any measured rate is artificial and attributed to changes in the temperature of the cooling water for the QCM. We use a closed system for the cooling water for all the MBE components. This system uses a heat exchanger to couple the cooling power of the building cooling water to this closed system. The cooling power is set by controlling a valve that throttles the flow of the building cooling water on one side of the heat exchanger. These rate oscillations where observed when the closed water system temperature was set lower than the building cooling water and therefore the system had no ability to regulate the temperature. The temperature fluctuations in this case were less than 1 °F and correspond to a changes of 5% in the measured copper rate. Copper is must more sensitive to these kinds of fluctuations because it has a much smaller mass than lanthanum and therefore produces smaller changes in the frequency of the QCM for a similar number of atoms. The solution in this case was to set the temperature of the closed cycle water cooling system 5 °F higher, from 60 °F to 65 °F, where it could more reliably maintain a steady temperature.

The temperature of growth is another critical parameter. Here the challenge has more to do with knowing the actual temperature of the sample than overly precise control of that temperature. We have two different means for measuring the temperature of the substrate, each with their own drawbacks. The first is a thermocouple situated in a position above the substrate heater. For reference, the sample substrate is located below this heater. The position of the thermocouple is designed to be a distance away from the heater that is equavalent to the distance the sample is away from the heater but in the opposite direction. The assumption is that these two positions are at similar temperatures and therefore the thermocouple is approximately reading the substrate temperature. Obviously, this assumption is only true up to point and therefore the temperature we read

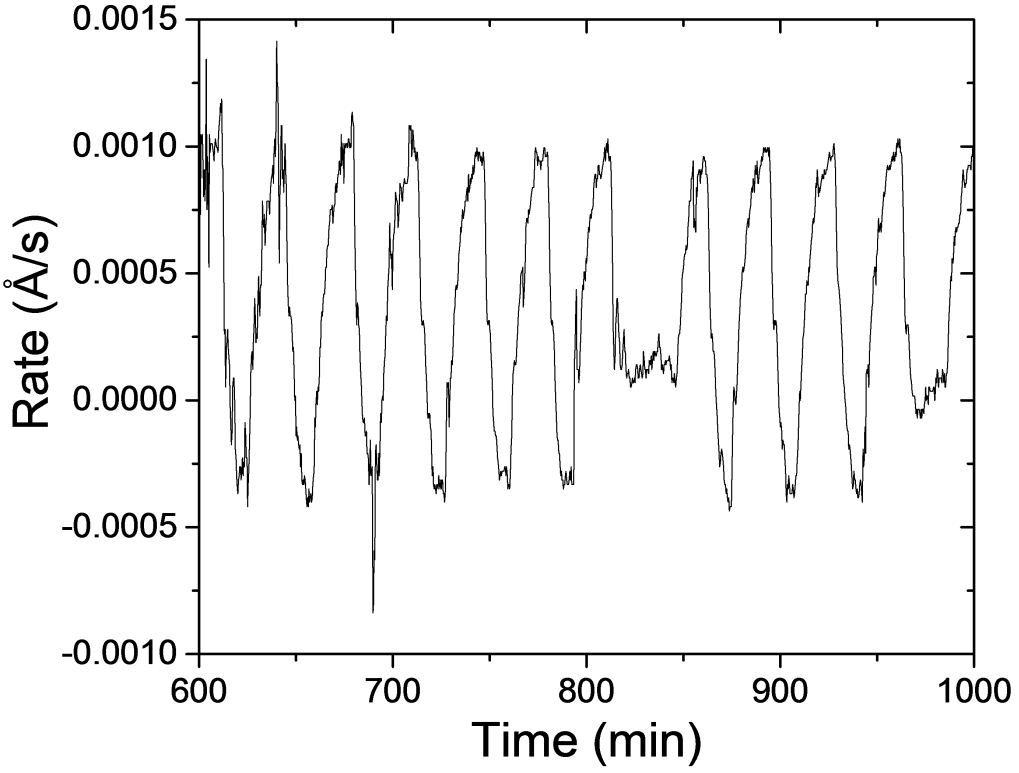

Figure 2.3: Cu rate measured with the shutter closed so no actual material was being deposited on the QCM. The observed oscillations are due to fluctuations in the temperature of the cooling water for the QCM.

from the thermocouple at best gives us a rough estimate of the actual substrate temperature during growth. The second temperature measurement is done using a pyrometer. We use a Williamson Pro 92-38 dual wavelength pyrometer. This is mounted externally on the MBE chamber and measures through a window pointed at the substrate. The actual values measured by the pyrometer and thermocouple typically disagree by about 80 °C, with the pyrometer always reading higher. With this discrepancy we operate on the assumption that both values have an

uncertainty of roughly this magnitude. We control the temperature of the substrate by applying a fixed voltage across the heater of 20-30 V. As the heater oxidizes over time its resistance steadily increases and one needs to apply higher and higher voltages to maintain a constant applied power. The typical lifetime of a substrate heater is approximately 30 sample growths.

2.2 Substrate Characterization

Starting with a high quality substrate is essential for growing high quality superconducting La_2CuO_{4+x} thin films. We use $SrLaAlO_4$ as the substrate material. This material was chosen because it has a good lattice match to bulk La_2CuO_{4+x}. A summary of the lattice mismatch between the a and b lattice parameters of bulk La_2CuO_{4+x} and $SrLaAlO_4$ is shown in table 2.1. It is worth noting that while bulk La_2CuO_{4+x} has an orthorhombic structure we are growing on a tetragonal substrate and we do see epitaxial growth with the film locked to the a and b lattice constants of the substrate, which means the films we produce are tetragonal. All the films presented in this thesis where grown on $SrLaAlO_4$ substrates purchased from MTI Corp. The two primary ways in which we quantify the quality of the substrates are through atomic force microscopy (AFM) and x-ray diffraction rocking curves. A typical AFM scan of a bare substrate is show in Fig. 2.4. This substrate was not treated in any way prior to this AFM measurement and it is surprising that a substrate straight out of the box like this displays a distinct terrace structure. The terrace structure comes from the slight miss-cut of the substrate. From previous experience in our lab we need to go through an involved etching and annealing procedure to produce similar features on $SrTiO_3$ (STO) substrates. The histogram, also shown in Fig. 2.4, displays peaks associated with each flat

terrace step. The spacing between these peaks gives us 5.5 Å as a measure of the step height, which corresponds to approximately 1/2 the unit cell for $SrLaAlO_4$. Like La_2CuO_{4+x}, the unit cell of $SrLaAlO_4$ consists of a pair of nearly identical material stacks and there is a natural cleavage plane at the half unit cell point. The RMS roughness of the substrate is 3.5 Å measured over a 1 μm square, which corresponds to roughly 1/4 of a unit cell of La_2CuO_{4+x}.

Lattice Constant	$SrLaAlO_4$ (a = b)	La_2CuO_{4+x} (x = 0.12) [6]
a	3.754 Å	3.774 Å
b	3.754 Å	3.825 Å
c	12.630 Å	13.197 Å

Table 2.1: Lattice parameters for SLAO and LCO.

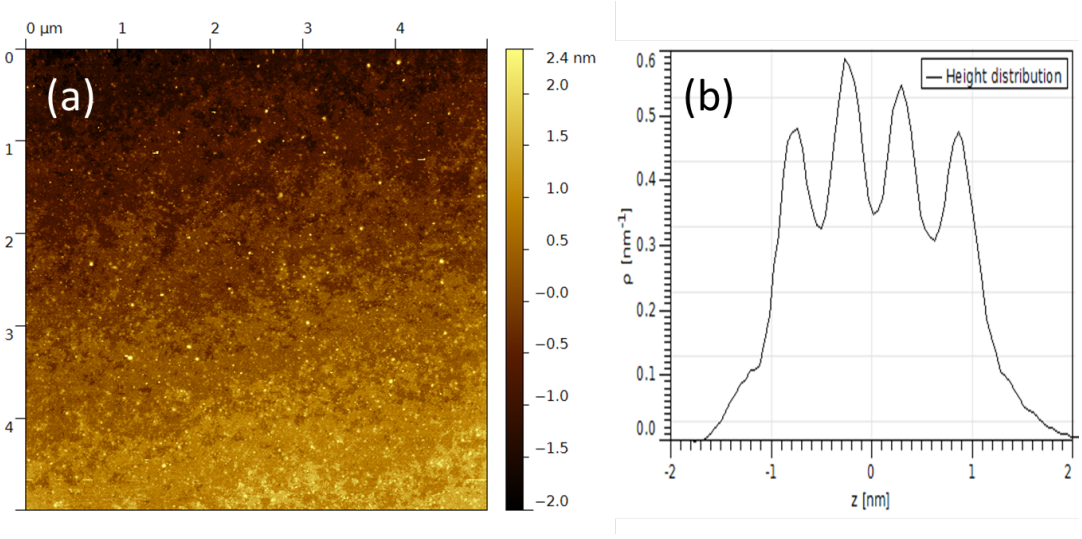

Figure 2.4: (a) AFM scan for a typical $SrLaAlO_4$ substrate showing distinct terrace steps. (b) Histogram of AFM image showing peaks associated with each terrace step. The distance between peaks is 5.5 Å, which corresponds with 1/2 unit cell step heights.

The second method we use for characterizing the substrate quality is x-ray diffraction rocking curves. A crystal substrate can be composed of many smaller

crystals that nucleated separately during the formation of the crystal. The rocking curve gives us a measure of the mosaic spread of all these separate parts of the substrate. For a well aligned crystal the rocking curve will produce a sharp peak while a substrate with many separate crystals all out of alignment will produce a broader peak. Fig 2.5 shows an intensity vs ω scan with the x-ray diffractometer aligned to the 006 plane of the substrate. The measured width of the peak of 0.004 degrees indicates the individual crystals in the substrate are well aligned.

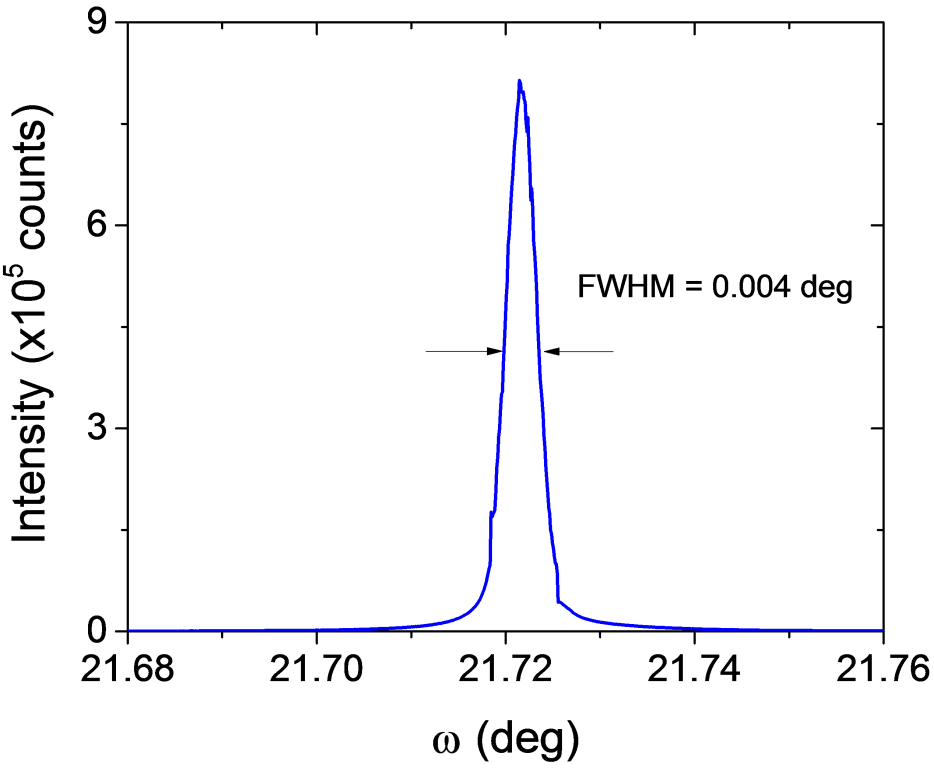

Figure 2.5: Rocking curve for a typical $SrLaAlO_4$ substrate measured at peak associated with the 006 plane. The FWHM of 0.004 degrees indicates that this is a well aligned crystal.

Based on our AFM and x-ray measurements of the substrates supplied by MTI

corp we conclude they are of good quality. With a good crystal substrate to use as our pattern for epitaxially growing La_2CuO_{4+x} thin films our next step is to examine the quality of the film deposited on top of this substrate.

2.3 Sample Characterization

We have several methods for characterizing the quality of the samples grown by MBE. During the growth we can monitor the crystal structure of the film using reflection high-energy electron diffraction (RHEED). RHEED provides us with information about the in-plane lattice parameters and the smoothness of the sample. After the sample is grown we use x-ray reflectivity (XRR), x-ray diffraction (XRD), atomic force microscopy (AFM), and Rutherford Back Scattering (RBS) to further characterize the properties of the film. XRR provides us with a measure of the film thickness as well as the roughness of both the top and bottom surfaces. XRD probes the c-axis lattice parameter. AFM is another measure of the sample roughness and RBS is way of checking the film stoichiometry. We use all this information to characterize the overall film quality and feed this information back into the processes to optimize the growth conditions.

We monitor the sample quality during the growth using RHEED. We use an RH-35 system from STAIB instruments and KSA-400 software. For a perfect 2D thin film the RHEED signal would be a set of vertical streaks where the spacing between the streaks is the reciprocal coordinate for the in-plane lattice parameter. For a film where there is growth out of the surface the streaks will break up into a pattern in the vertical direction. The streaks will form distinct spots indicating the growth is more three dimensional than two dimensional. Three dimensional or out of plane growth can occur if the stoichiometry of the film is incorrect or if the

growth temperature is too high or too low. The top image of Fig. 2.6 shows the RHEED signal for a typical La_2CuO_{4+x} film were the growth temperature and film stoichiometry were correct. The lower two images in Fig. 2.6 show the RHEED patterns for films where their was either an excess of Cu or and excess of La. We can see that in both of these off stoichiometry cases the ideal pattern of vertical streaks breaks up in to distinct spots. This indicates that there are clusters of binary oxides growing out of the surface of the film instead of spreading uniformly across the surface. It is important to note that for both of the off-stoichiometry cases shown in Fig. 2.6 the excess of Cu or La was greater than 10%. It is possible for the stoichiometry to be incorrect but in a less severe way where it does not show up in the RHEED pattern but still produces poor quality films in terms of resistance and T_c. We use RHEED as a first measure of film quality but it is not as sensitive as measuring the transport properties of the film.

After we remove the film from the MBE chamber we use x-rays to probe the structure of the film. We measure both XRR and XRD. A typical XRR is shown in Fig. 2.7. XRR is performed at small angles where we can think of the film as a continuous unit and the information we derive comes from the x-rays probing the different index of refraction of the film as opposed to the air and the substrate. This means that XRR can probe the thickness of the film and the quality of the top and bottom surfaces. For the 4 unit cell La_2CuO_{4+x} film show in Fig. 2.7, we fit the x-ray reflectivity data using GenX to determine the film thickness to be 47.3 Å, the roughness at the sample substrate interfaces to be 3 Å, and the roughness at the sample air interface to be 8 Å. We can take this same 2θ x-ray scan to wider angles where the x-ray beam will diffract off successive layers of the film and use this to probe the c-axis of the film. The wide angle diffraction scan in Fig. 2.7 shows the 004 peak for the La_2CuO_{4+x} film as well as a small

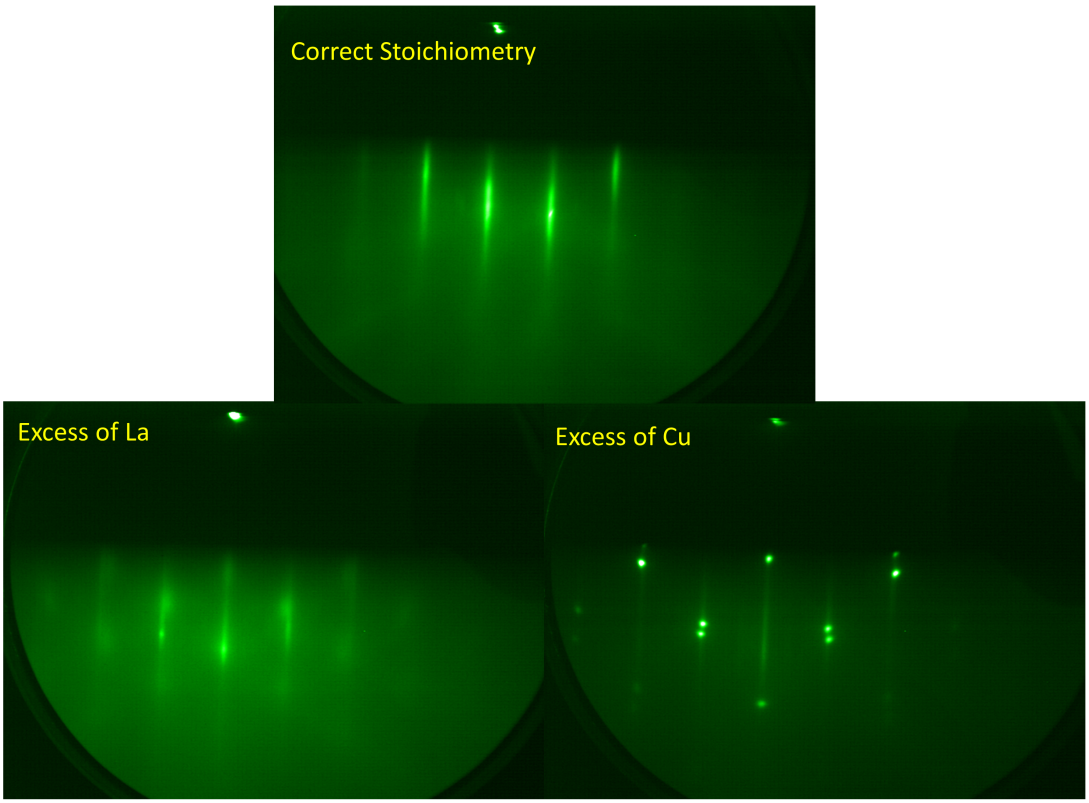

Figure 2.6: The RHEED pattern of a film grown with the correct stoichiometry as well as the cases where there is either an excess of Cu or an excess of La.

thickness fringe which is an indicator that this film is of good quality. The center of the peak provides a measure of the c-axis lattice parameter, which is 13.3 Å, and the width of the peak provides us with a measure of the film thickness, which is 44.5 Å. We can compare the lattice parameters of the La_2CuO_{4+x} film to the bulk parameters in Tab. 2.1. The a and b parameters are fixed epitaxially to the substrate and therefore we have a compressive in-plane strain. As a result of this in-plane strain, the c-axis increases from 13.2 Å to 13.3 Å.

An alternative way to measure the roughness of the film is using AFM, and a typical AFM scan of a 4 unit cell La_2CuO_{4+x} sample is shown in Fig. 2.8. The

RMS roughness of this sample is 3 Å. The important comparison to keep in mind when examining the roughness of the film is how it compares to the thickness of a unit cell and the overall thickness of the film. The roughness quantified by AFM and XRR range from 1/4 to 2/3 of a unit cell where the films we will examine in this study are 3-4 unit cells in thickness. This means that even if the interior of the film is perfect the rough top and bottom surface still make up a significant fraction of the whole and we will see in Sec. 5.2 that this puts these film into a strong scattering limit.

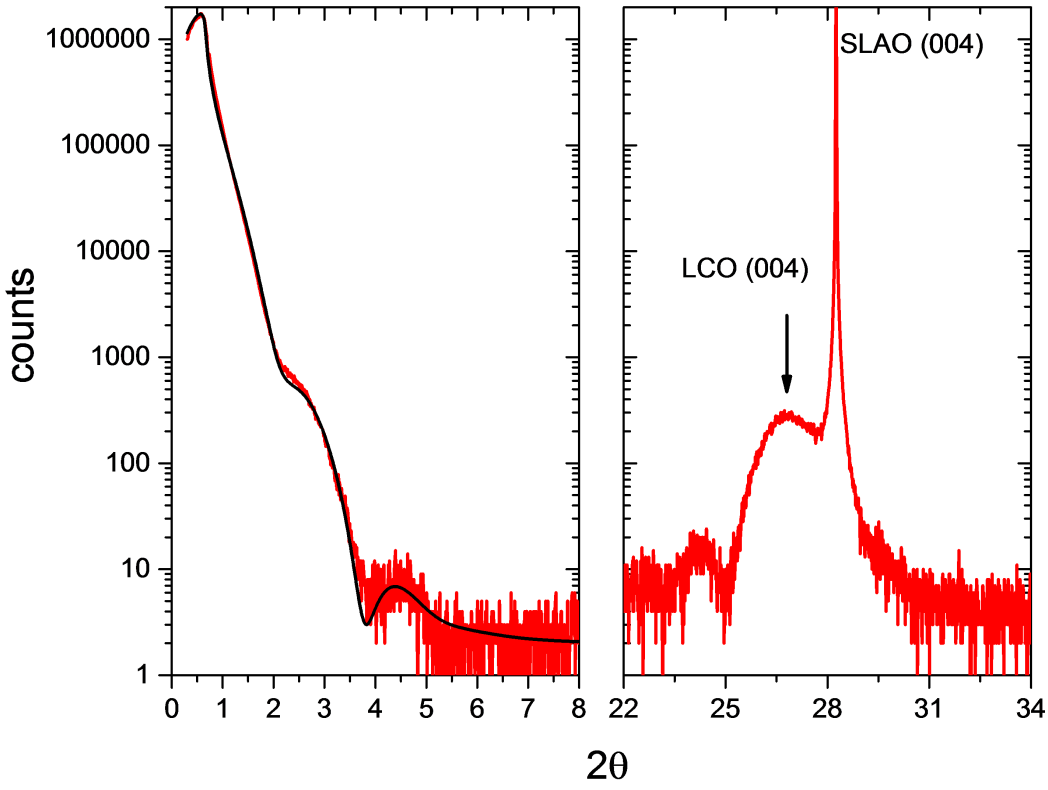

Figure 2.7: X-ray reflectivity (left panel) and diffraction (right panel) for a 4 unit cell LCO film.

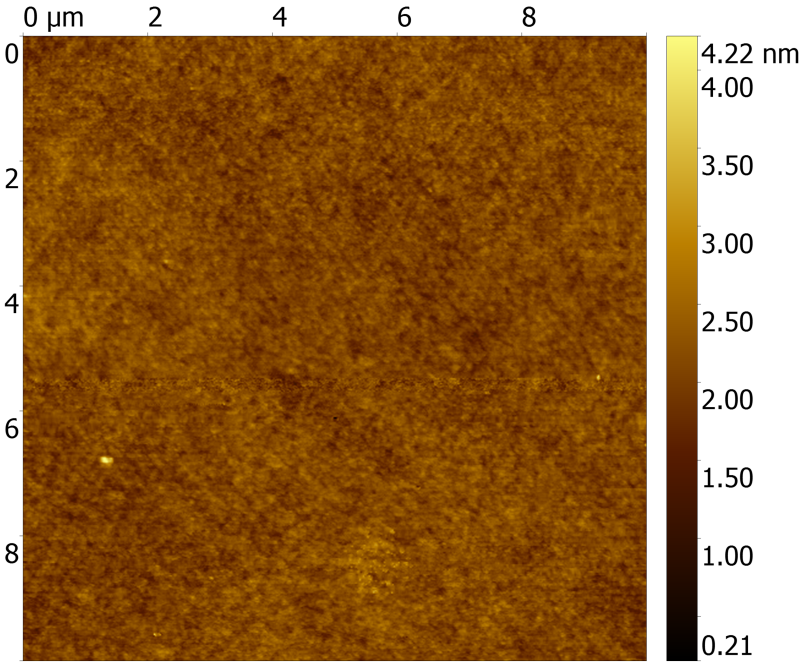

Figure 2.8: Typcial AFM scan of a 4 unit cell La_2CuO_{4+x} sample showing extremely smooth surface over a wide area of 10 μm^2. The RMS roughness of this sample is 2 Å.

A key component of growing a good quality film is having the right film stoichiometry. We can use Rutherford Back scattering (RBS) to determine the ratio of number of La to Cu atoms in our film and check whether we are indeed depositing them in a 2 to 1 ratio as we intend. Fig. 2.9 shows a typical RBS spectrum for a 4 unit cell La_2CuO_{4+x} film grown on an MgO substrate. The smaller peak is from Cu and the larger peak is from La. MgO is used for this measurement because the La in an $SrLaAlO_4$ substrate would produce a strong step in the RBS spectrum making it difficult to separate the La signal that is coming from the substrate from the La signal that is coming from the film. We determine the number of atoms for each element by integrating the area under the peak and take that area divided by the square of the atomic number for the element associated with

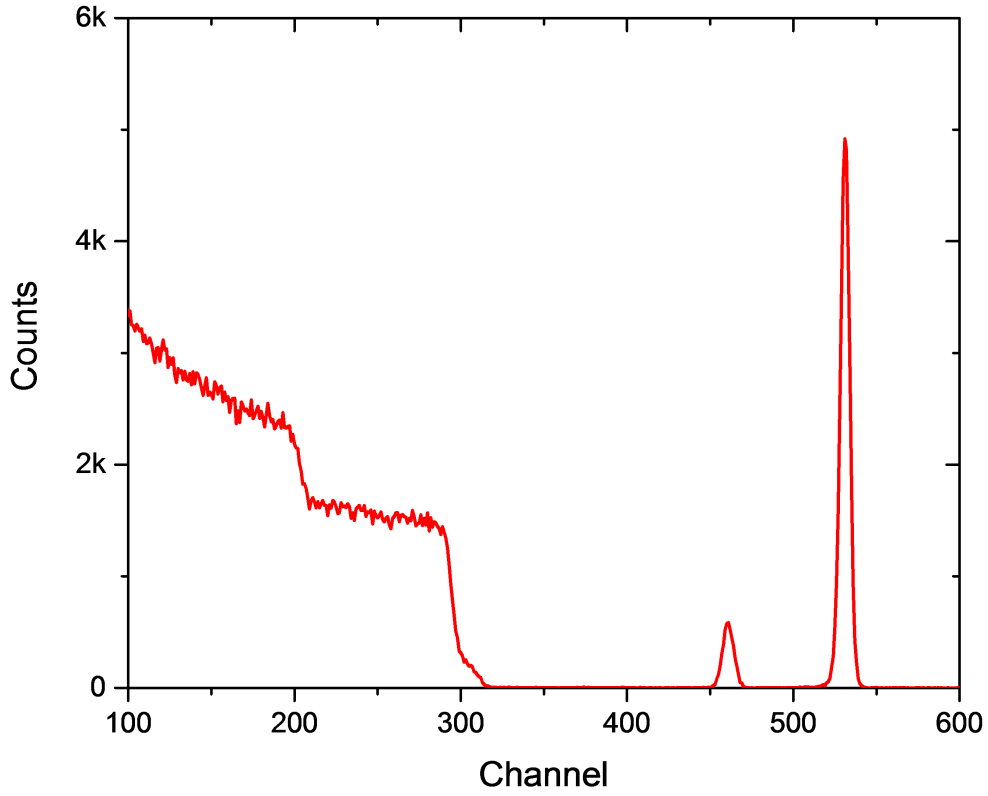

Figure 2.9: Typcial RBS scan for a 4 unit cell La_2CuO_{4+x} film grown on an MgO substrate. The smaller peak is from Cu and the larger peak is from La.

that peak. We do this for both the La and Cu peak and then take the ratio of those two quantities to determine the stoichiometry of the film.

The final and most sensitive check of film quality is the resistance. Section 4.1 will cover the procedure we use for making this measurement in more detail. Here we would simply like to use the resistance of samples grown with different thicknesses to get an estimate of the number of dead layers in our films. A dead layer is a thickness of film where the properties of the film are different from the bulk. We are growing our La_2CuO_{4+x} films on $SrLaAlO_4$ substrates where the lattice mismatch is detailed in Table 2.1. Fig. 2.10 shows the sheet resistance vs

temperature for both a 2 unit cell and a 3 unit cell film. The sheet resistance of the film is related to the intrinsic resistivity of the material by $R_s = \rho/t$, where R_s is the sheet resistance, ρ is the resistivity, and t is the film thickness. If there were no dead layers in the film we would expect the resistance of the 2 unit cell film to be 50 % larger than the resistance of the 3 unit cell film. We see that instead the resistance of the 2 unit cell film is approximately 7 times larger than the resistance of the 3 unit cell film. Assuming the resistivity of a dead layer is infinite we can estimate the thickness of the dead layers in these films to be approximately 1.4 unit cells. We can also account for the 40 Å thickness of the 3 unit cell film to determine the resistivity of the film at 400 $\mu\Omega$cm. This is 2-5 times larger than typical bulk resistivity of similar materials[7].

We have outlined the procedure for using ozone assisted MBE to produce La_2CuO_{4+x} thin films. We must take care to precisely control the material flux rate of the copper and lanthanum sources. Our limited ability to hold these rates constant is the primary limit on repeatability of this growth procedure. We use $SrLaAlO_4$ supplied by MTI Corp. which based of our measurements of AFM and x-ray diffraction rocking curves are of high quality. In fact, with no surface preparation at all we see distinct terrace steps in these substrates. Both during the film growth and after the film is removed from the MBE chamber we use a variety of characterization tools to more fully understand the material properties of these films. Our main tool during the growth is RHEED which shows epitaxial growth with the a and b lattice locked to the substrate. After growth we can characterize the film roughness both top and bottom using a combination of XRR and AFM to see that even in the best films there is a surface roughness on the order of 1/4 to 2/3 of a unit cell. We will keep this quantity in mind when we are discussing the penetration depth measurements in Sec. 5.2 where we will conclude

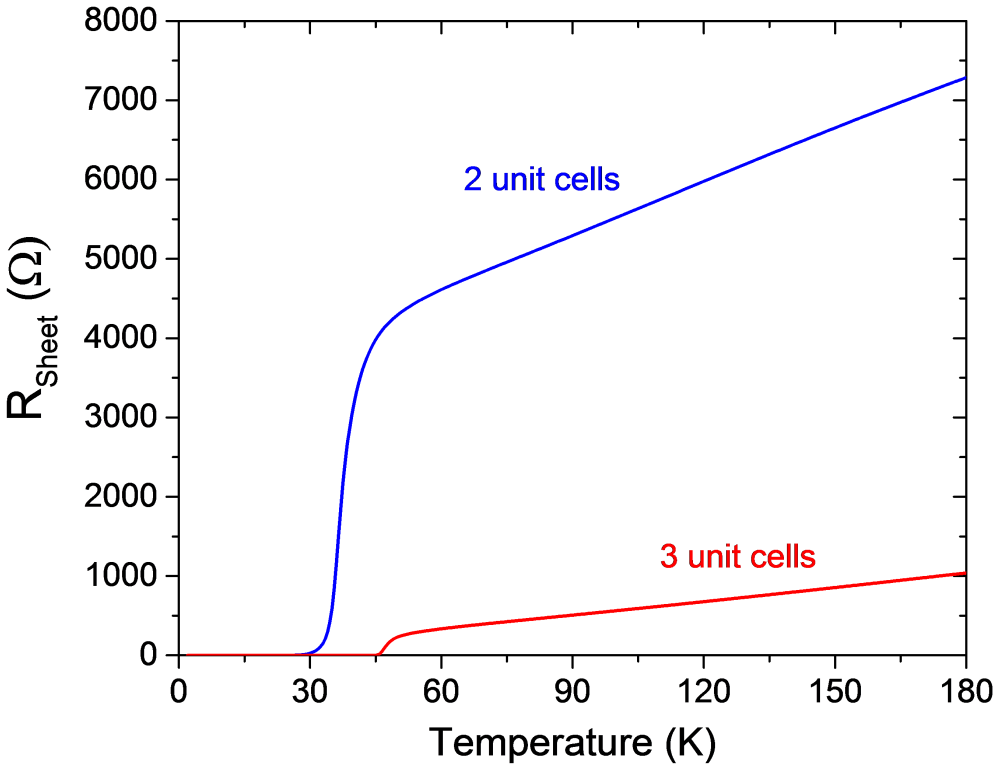

Figure 2.10: Resistance vs temperature for 2 unit cell and 3 unit cell La_2CuO_{4+x} films. The fact that the normal state resistance of the 2 unit cell film is 7 times the resistance of the 3 unit cell film implies that there are 1-2 dead layers in a typically grown film.

that these films are in the large scattering limit. Now that we have demonstrated how we produce a strong superconducting sample near optimal doping our next goal is to adjust the doping and for that we will use ionic liquids.

Chapter 3

Ionic Liquid Gating

Our goal is to systematically explore how doping effects the properties of the high temperature superconductor La_2CuO_{4+x} (LCO). Typically this would require us to grow a whole series of samples at a range of different dopings. While this is a perfectly reasonable strategy it does require a great deal of time and assumes a precise level of control over the material growth. For the work presented in this thesis we will use an alternative technique for electrostatically adjusting the doping of our material that will make use of ionic liquids.

The idea of electrostatically modulating the carrier concentration of complex oxides has been of great interest for many years [8, 9]. And the idea of using a conventional field effect device to adjust the doping of high-T_c materials has been an active field over the past several years [10, 11, 12, 13]. Within our own lab we have used a gate and a conventional dielectric to study the superconductor-insulator phase transition in quench condensed bismuth films [14]. The conventional implementation of this device involves using a solid dielectric and metal gate to adjust the doping of a material. For example, one can use strontium titanate, which has a large dielectric constant at low temperatures, as the substrate for depositing a

material and then adding a gate electrode on the opposite side of the substrate. By applying a voltage between the gate and the sample one can adjust the doping within the sample. The problem with a conventional solid dielectric and gate is the magnitude of changes in carrier concentration that can be produced. Even if one uses a material like strontium titanate, which has a very large dielectric constant, as the dielectric material one can at most produce changes in carrier concentration of up to $1x10^{13}$ carrier/cm^2. For a thin film, where there is only a single copper oxygen plane a change $1x10^{14}$ carrier/cm^2 would be just enough to take the sample from the top of the superconducting dome to the fully undoped state. For LCO this would be a film that is 1/2 of a unit cell thick because there are two copper oxygen planes in each unit cell. The thinnest films we can grow which exhibit homogeneous superconducting properties are 3 unit cells thick, which contain 6 copper oxygen planes. This means having a tool that can produce changes in carrier concentration on the order of $1x10^{15}$ carrier/cm^2 is needed. Thankfully ionic liquid is just such a tool.

An ionic liquid is a combination of compounds that form a molten salt at relatively low temperature. For example, if we take table salt up to 801 °C it will melt into a liquid with positive sodium ions and negative chloride ions. The ionic liquid we will use for the work presented here is N,N-diethyl-N-(2-methoxyethyl)-N-methylammonium bis(trifluoromethylsulphonyl-imide (DEME-TFSI). Like the example of table salt at high temperatures this compound forms a liquid composed of DEME cations and TFSI anions with the primary difference between table salt and DEME-TFSI being their melting points. Whereas table salt needs to be heated up to high temperatures to melt, DEME-TFSI melts at around 200 K, which is well below room temperature. The rough lateral scale of both the DEME and TFSI ions is 1 nm.

Ionic liquids are a powerful tool for modulating the carrier concentration of materials and recent studies using this tool to induce superconductivity in strontium titanate[15] sparked a great deal of interest in this field. However, the idea of modulating the properties of high temperature superconductors with ionic liquids goes back more than 20 years [16, 17] with more recent examples in $La_{2-x}Sr_xCuO_4$ [18], $YBa_2Cu_3O_{7-x}$[19, 20], LCO[21], and $Pr_{2-x}Ce_xCuO_4$ [22]. The work presented here is an extension of the work cited on LCO.

Figure 3.1 shows schematically how the setup involving ionic liquid works. Both the sample and a gate electrode are immersed in the ionic liquid, which for our experiments will be DEME-TFSI. By applying a voltage between the gate and the sample we can induce a buildup of ions on the surface of the film. This layer of ions on the surface of the film induces image charges in the sample of the opposite sign. One way to think of this procedure is that we are building a pair of capacitors at both the gate and the sample surface. Because the effective spacing between the plates of this capacitor are the size of the ion, which is on the order of a few nanometers, we expect this to be be a large effective capacitance and to induce large changes in the carrier concentration of the sample. The is clear when we look at the general expression for the capacitance where $C = \epsilon_0 \epsilon_r A/d$ and the capacitance increases with as the distance between the plate is minimized. We can also think about the depth within the material over which we expect to effect changes. A simple estimate for the depth over which electrostatic fields will be screened out is the Thomas-Fermi screening length defined as

$$\lambda_{TF}^2 = \frac{\hbar \pi \epsilon_r \epsilon_0}{4 m_e e^2} \left(\frac{3\pi^2}{n} \right)^{1/3}.$$

If we use $\epsilon_r = 20$[13] and $n = 2.5 \times 10^{21}$ cm^{-3}, we estimate $\lambda_{TF} = 0.4$ nm. This is roughly one tenth of the thickness of the thinnest films we can produce. We are able to fully modulate the properties of these films which implies there is likely

more than electrostatic changes at play.

In this picture we are assuming that all the changes effected in the sample are due to electrostatic effects caused by this capacitor type of charging. In this idealized picture the changes in doping of the material would be fully reversible, and the primary source of disorder would be from the random distribution of the ions on the surface of the material. In practice we see that we also affect the intrinsic chemical doping of the material. This still has the advantage of being an *in-situ* method which does allow for precise control of the doping and offers a degree of reversibility.

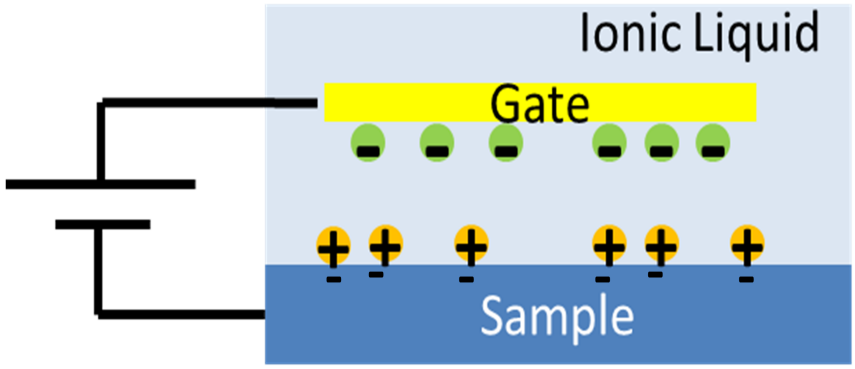

Figure 3.1: A schematic of the use of ionic liquid to adjust the doping of a material. Both the sample and a gate electrode are immersed in the ionic liquid. In this case we are applying a positive gate voltage which attracts negative ions to the gate and positive ions to the sample surface. This layer of positive ions on the surface of the material acts like a nanoscale capacitor and induces electrons (removes holes) from the material.

Of the many challenges associated with using ionic liquids sorting out electrostatic effects from electrochemical effects can be key. Previous work on gold films [23] shows that much of the conductivity modulation exhibited by ionic liquid gating is actually due to a reversible oxidation reaction at the film surface. Previous work on VO_2 [24] shows that ionic liquid gating can induce oxygen vacancies for a positive polarity applied to the gate, which account for much of the induced carriers rather than electrostatic forces. Also in VO_2 it was shown that ionic liquid can induce reversible structural changes in this material [25]. Previous STEM studies on $La_{1/3}Sr_{2/3}FeO_3$ show that the addition of ionic liquid can actually remove material from the surface of the sample and incorporate it into the bulk of the ionic liquid [26]. One strategy that has been proposed for minimizing these chemical effects is putting a flake of boron nitride between the sample and the ionic liquid to act as as a shield[27]. While this flake can suppress the chemical effects it also decreases the effective capacitance of the device by increasing the spacing between the ions and the sample.

Over the next three sections we will explore in detail to what degree we are dealing with an idealized electrostatic charging process and to what degree there are chemical effects taking place. Section 3.1 will look at what happens when we simply add ionic liquid to the surface of an La_2CuO_{4+x} film without applying a gate voltage. In Sec. 3.2 we will discuss to what degree the crystal structure is affected by ionic liquid. Finally, in Sec. 3.3 will look at a couple of examples of what happens when we try to reverse the gate voltage and return a sample to it's initial state.

3.1 Sample Degradation

In a perfect scenario, all the changes induced in our sample would come solely from applying a gate voltage between the sample and gate electrode and these changes would be perfectly reversible. For some material systems this may be largely true, but for the work we present here involving LCO and DEME-TFSI this is not explicitly true. The choice of DEME-TFSI was arbitrary and based on the previous work in our lab and other groups performing similar experiments. It is likely that is is not the optimal choice. The first example of this kind of non ideal behavior comes from simply putting ionic liquid on the surface of the sample. Figure 3.2 shows resistance vs temperature for a 4 unit cell LCO film before and after the addition of ionic liquid. In this case, the ionic liquid was applied to the surface of the sample at room temperature and then the sample was cooled down to 200 K, which is below the melting point of the ionic liquid. The time to cool down was approximately 30min. We see that simply adding ionic liquid to the surface of the sample increased the normal state resistance and decreases T_c. There is nothing about these changes that can be attributed to electrostatic charging because the gate voltage was left at zero throughout this experiment. It is important to note that while the applied voltage is set to zero this does not force the electrochemical potential between the sample and the ionic liquid to zero. What is more, we can also look at the Hall effect in this same sample. Figure 3.2 shows the transverse resistance, R_{xy}, as a function of the an applied perpendicular magnetic field, measured at 180K. This transverse resistance is inversely proportional to n, the carrier concentration in the material. If we assume a simple Drude model with only a single type of charge carrier for the conductivity of our film as $\sigma = \frac{ne^2\tau}{m}$, we would expect the sheet resistance to

change proportionally to the transverse resistance if we are primarily changing the number of carriers. The ratio of the sheet resistance before and after the addition of ionic liquid is 0.7, and the ratio of the transverse resistance at 9 T before and after the addition of ionic liquid is also 0.7. This means that the changes in resistance are primarily explained by changes in doping and therefore we expect in this case we are producing a minimal change in the disorder of the material.

We can understand this increase in resistance by considering the role of the interstitial oxygen in this material. The as grown material La_2CuO_{4+x} films we use for our studies are at a doping of approximately x=0.12. This doping is estimated by comparing the transition temperature measured in our films to those in the literature[28, 6]. The excess oxygen resides in interstitial spaces between the lanthanum oxide layers. It is known from previous work that these interstitial oxygen atoms are mobile down to 200 K [29]. What is more the phase diagram of La_2CuO_{4+x} has miscibility gaps depending exactly on the concentration and structural staging of the interstitial oxygen. FigureWe can experiment with the interstitial oxygen stability by examining a film where we do not add ionic liquid and instead just increase the temperature. We see that just increasing the temperature to slightly above room temperature in a vacuum environment we can steadily increase the resistance and reduce T_c of a LCO film. Figure 3.4 shows the results of warming a 3 unit cell La_2CuO_{4+x} film to 340 K. We see that the resistance increases at a faster and faster rate as the temperature is increased. We interpret this result as the interstitial oxygen steadily leaving the sample, reducing the doping and therefore increasing the resistance of the sample.

Based on this result we conclude that going to lower temperatures should decrease this effect. So there is a chance that keeping the ionic liquid and sample below some temperature we can eliminate the steady loss of oxygen that we see

at higher temperatures. We need to warm the liquid to 240 K in order for the ions to be mobile and effect changes in the sample using the gate, which puts a minimum on how low we can keep the ionic liquid and sample system. We tested the addition of ionic liquid at 240 K to see if this steady loss of interstitial oxygen is still a problem at these reduced temperatures. We rigged up a setup inside the PPMS where we could load both the sample without ionic liquid and a bucket containing the ionic liquid. We cooled both the sample and bucket down to 240 K and then pulled a string to tip the bucket and pour the ionic liquid on the sample. Figure 3.5 show resistance vs temperature for the sample first without ionic liquid and then for a series of steps after the ionic had been added at 240 K. Each step consisted of warming the sample and ionic liquid to 240 K and waiting for 1 hour. We see that even if the sample and ionic liquid never go above 240 K there still is a steady increase in the normal state resistance. We conclude that there is always a steady loss of interstitial oxygen throughout the experiments presented here.

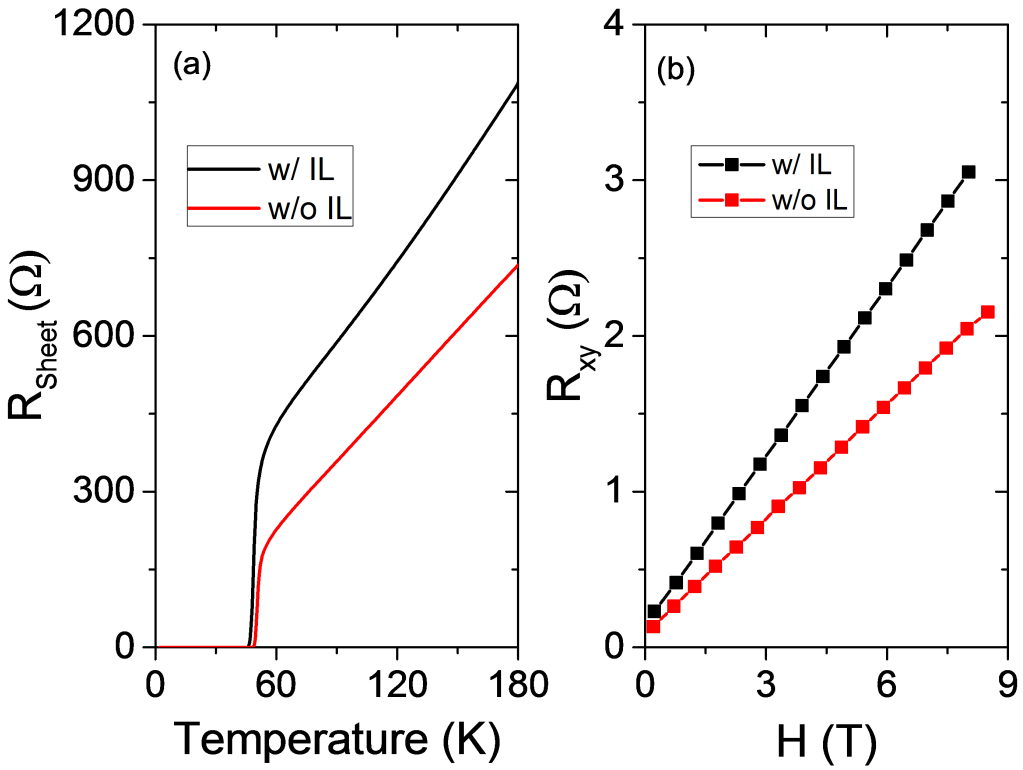

Figure 3.2: (a) The sheet resistance of a 4 unit cell La_2CuO_{4+x} sample before and after adding ionic liquid to the sample surface. In this case ionic liquid was added to the surface of the film at room temperature and then the whole setup was immediately cooled to below 200K over the course of approximately 30 min. We see both an increase in the normal state resistance and a decrease in T_c of the film after adding ionic liquid. (b) The transverse resistance of the film measured at 180 K both before and after the addition of ionic liquid. We see that change we see in the normal state longitudinal resistance is accompanied by a proportional change in the transverse resistance. This implies that while the changes cannot be electrostatic in nature because we are not applying any gate voltage, we are primarily affecting the doping of the material.

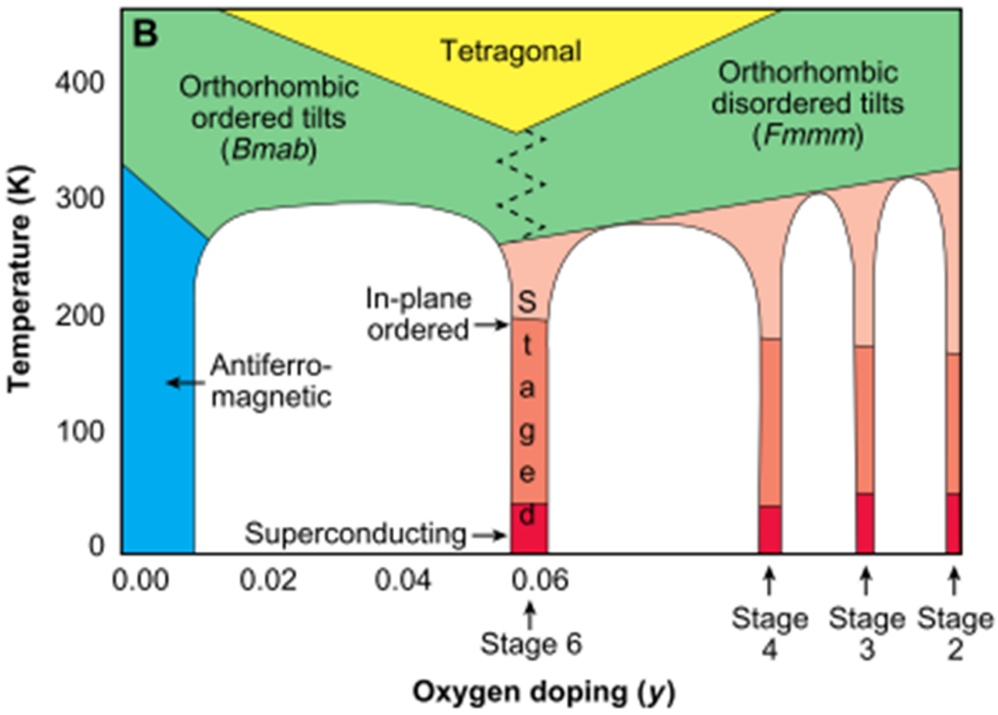

Figure 3.3: Phase diagram of La_2CuO_{4+x} taken from Wells *et al.*[28]. We can see that for the chemically doped material there are miscibility gaps where the material phase separates into regions with different interstitial oxygen staging and corresponding superconducting transition temperatures.

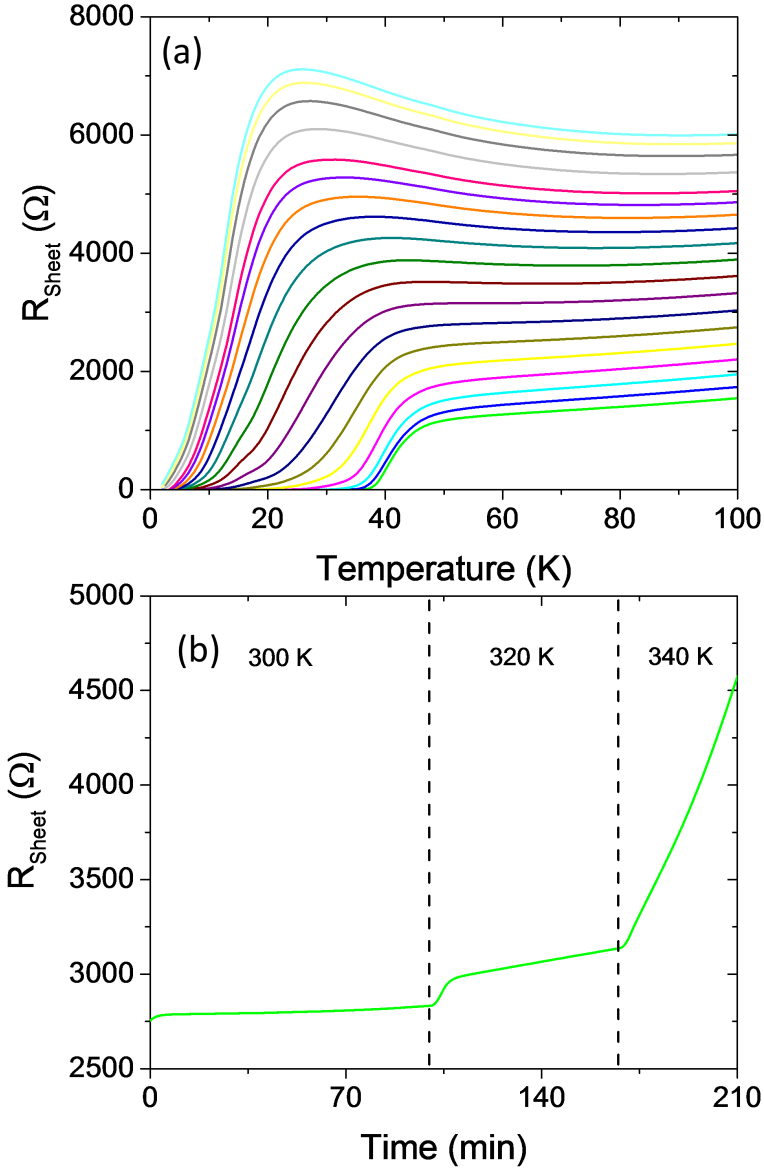

Figure 3.4: (a) A series of sheet resistance vs temperature curves for a 3 unit cell La_2CuO_{4+x} film, where each step involved warming the sample to 340 K in a vacuum environment and waiting for 20 minutes. (b) The sheet resistance vs time for this same sample. We see that the rate at which the resistance increases grows with temperature.

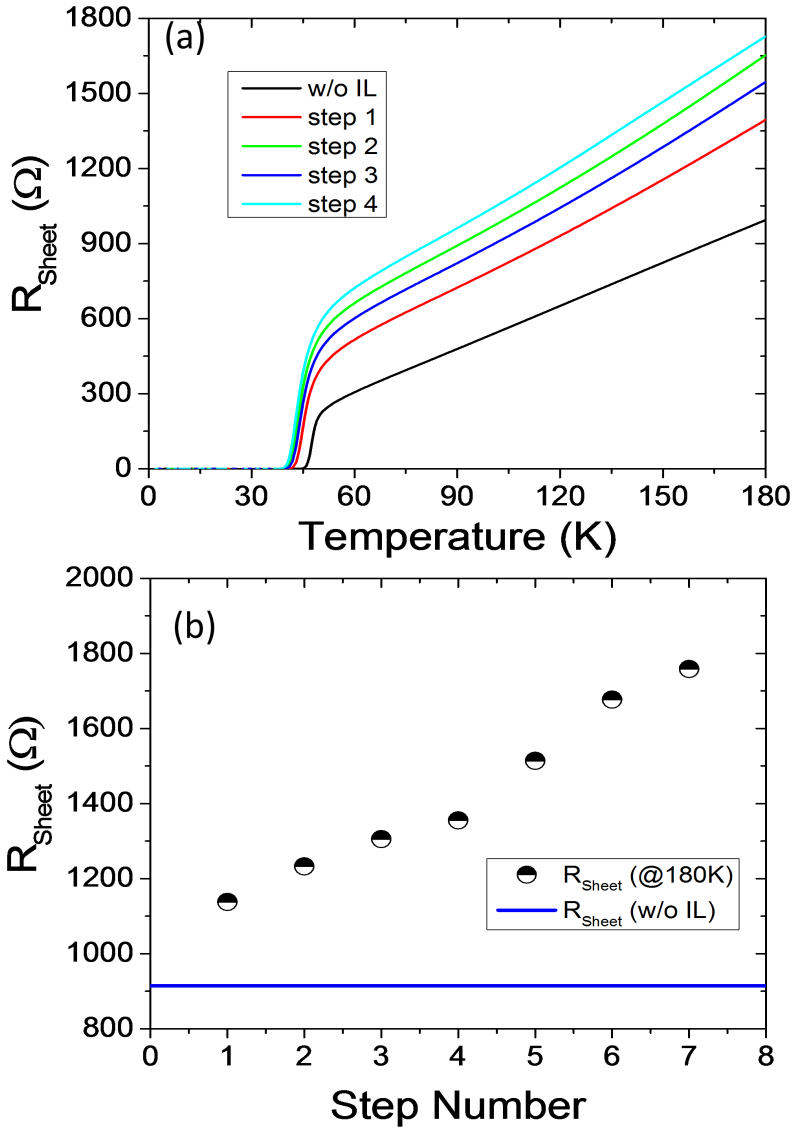

Figure 3.5: (a) The sheet resistance of a 4 unit cell La_2CuO_{4+x} sample after adding ionic liquid. The liquid was added to the surface of the sample while the sample and liquid where both inside the cryostat and stable at 240K. (b) Shows the sheet resistance at 180K for each measurement step continuing a couple of steps beyond the data in (a). For each step the sample with ionic liquid was warmed to 240K and held for 60 min and we see that the normal state resistance steadily increases with each step.

3.2 Structural Effects

Based on the results of the previous section we hypothesize that interstitial oxygens are leaving our samples over time and that this loss is accelerated by the addition of ionic liquid to the sample surface. If this is a correct conclusion there should be a corresponding change in the structure of these samples, namely the c-axis lattice parameter should shrink as we lose oxygen. Figure 3.6 shows the result of an experiment where we took an 8 unit cell LCO film to the Advanced Photon Source (APS) at Argonne National Lab. By using the strong flux of this synchrotron x-ray source we were able to measure x-ray diffraction patterns for the sample while ionic liquid was on the surface. We see that the addition of ionic liquid to the surface of the sample had two effects. The center of the peak associated with the (008) plane of the LCO film shifts to smaller L values, which would correspond to the c-axis growing. This is in contradiction with our interpretation that adding ionic liquid to the surface of the sample encourages the migration of interstitial oxygen out of the sample. The second effect we see is that the (008) peak, as well as the thickness fringes associated with this peak both broaden out. This broadening corresponds to the effective thickness of the sample shrinking. This could mean the ionic liquid is etching away the top surface of the sample or at least increasing the surface roughness. It also could correspond to an overall disordering of the film. It should be noted that all these measurements were performed at room temperature and repeating this experiment with better temperature control and at low temperatures are important next steps.

In addition to exploring the effect of simply adding ionic liquid to the surface of the sample we also would like to learn how applying a gate voltage to the ionic liquid adds to these effects. Figure 3.7 shows the results of additional

measurements using the APS and the same 8 unit cell LCO film as before. Here we alternate between applying positive and negative 2 V between the sample and the gate electrode and track the position of the peak associated with the (108) plane. We see that for positive voltages the peak shifts to larger L values which corresponds to a decrease in the c-axis lattice parameter. For negative applied gate voltages we see the peak shift to smaller L values which corresponds to an increase in the c-axis lattice parameter. If we assume that these shifts in magnitude of the c-axis are associated with adding or removing interstitial oxygen, we would say that applying a positive gate voltage is removing interstitial oxygen and applying a negative voltage is adding it back. Removing interstitial oxygen should also decrease the free carrier density in the material and this agrees with what we see from transport measurements, where applying a positive gate voltage increase the resistance of a sample. In addition to stepping up and down associated with the changes in gate voltage we also see a steady drift to smaller L values in agreement with the effect shown in Fig. 3.6. While these results are consistent with a picture where oxygen is the only chemically active element we can not rule out the possibility that the La:Cu ratio is being effect as well.

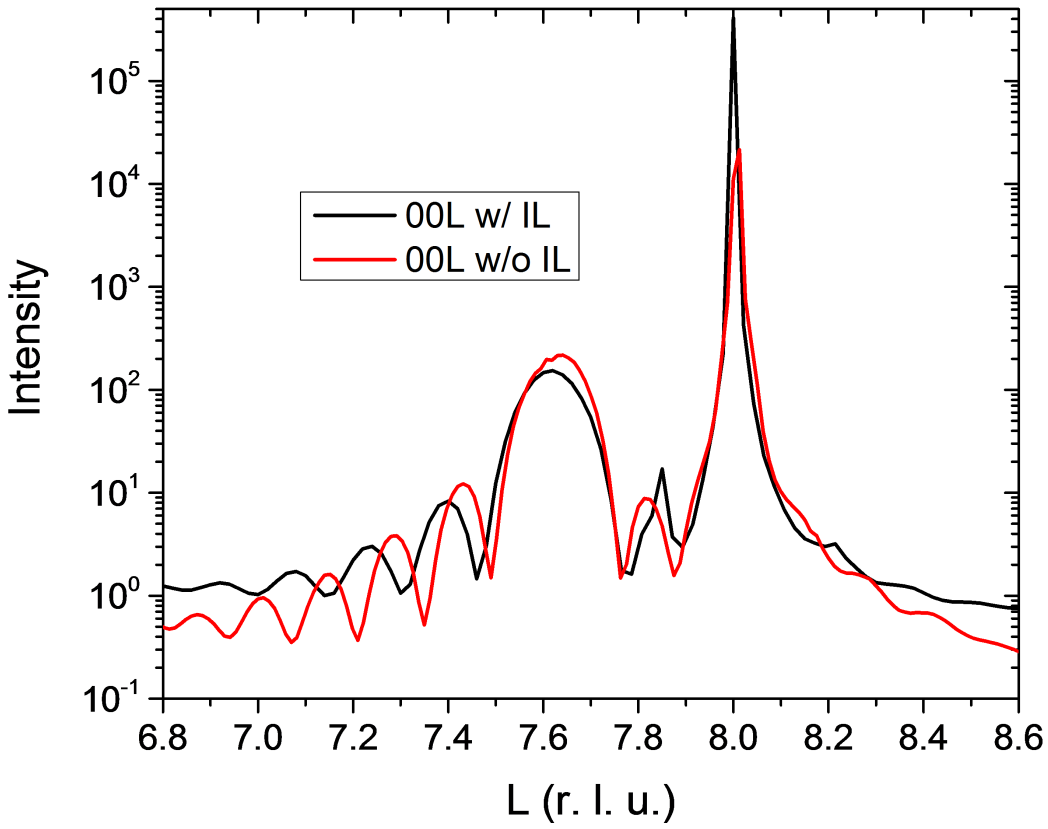

Figure 3.6: X-ray intensity as a function of the magnitude of the L reciprocal lattice vector calibrated to the substrate's c-axis spacing. The sharp peak is associated with the $< 008 >$ plane of the substrate. The broader peak is associated with the (008) plane of the sample. We see that adding ionic liquid to the sample surface slightly shifts the sample peak to smaller L values which would correspond to an increase in the c-axis. We also see that the fringes broaden with the addition of ionic liquid which correspond to the effective thickness of the sample shrinking, which could be due to a roughening of the sample surface.

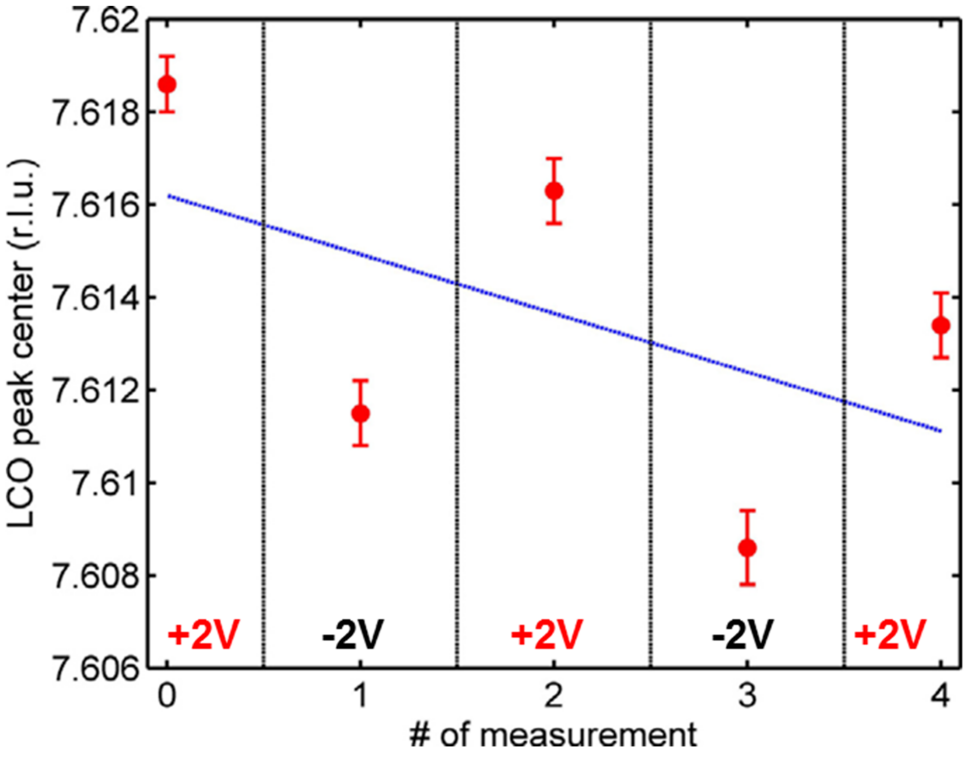

Figure 3.7: (Provided by Guichuan Yu). Tracking the center of the peak associated with the 108 plane in an 8 unit cell La_2CuO_{4+x} film as the gate voltage is alternated between positive and negative 2 V. We see that for positive gate voltages the peak shifts to larger L values, which corresponds to a decrease in the c-axis lattice parameter.

3.3 Reversibility

A final strategy for separating electrostatic from electrochemical effects it to check the reversibility of the ionic liquid doping procedure. A purely electrostatic process where there is a minimal number of trap states will be largely reversible, and returning the gate voltage to 0V should fully recover the initial state of the sample. Figure 3.8 shows a pair of examples where we attempted to reverse the ionic liquid doping procedure. We see that there is in fact a large hysteresis associated with the doping, in that returning the voltage to zero does not recover the initial state. It is only after applying a negative voltage that we recover something similar to the initial state. What is more, while we can return the sample to the a similar value of T_c, the sharpness of the transition has changed. For panel (a) the transition is broader on the return trip and in panel (b) the transition is sharper. Both of these results point to the fact that the doping is not uniform over the entirety of the sample. This could be due the size and shape of the charging electrode, which is smaller than and differently shaped than the sample. The sample is a plane and the gate is a coil of Pt wire. But we hypothesize that the small sheet resistance of the sample (< 10 kΩ) should force the ions to distribute themselves uniformly across the surface of the sample. The other possibility for nonuniformity would be a thickness dependent effect where the top surface of the sample is affected more strongly than the underlying layers.

We see that much of the change in LCO doped films using DEME-TFSI is not electrostatic in nature. The mobility of the interstitial oxygen in this material likely make this a particularly sensitive material to electrochemical effects some of which change the underlying crystal structure of the material. We also see that while returning the gate voltage to 0 V does not return the sample to it's initial

state we can produce a degree of reversibility by switching the sign of the applied gate voltage. Overall, we see that using ionic liquids to dope thin films of LCO is a powerful tool and we will further examine the potential of this tool in Chap. 5.

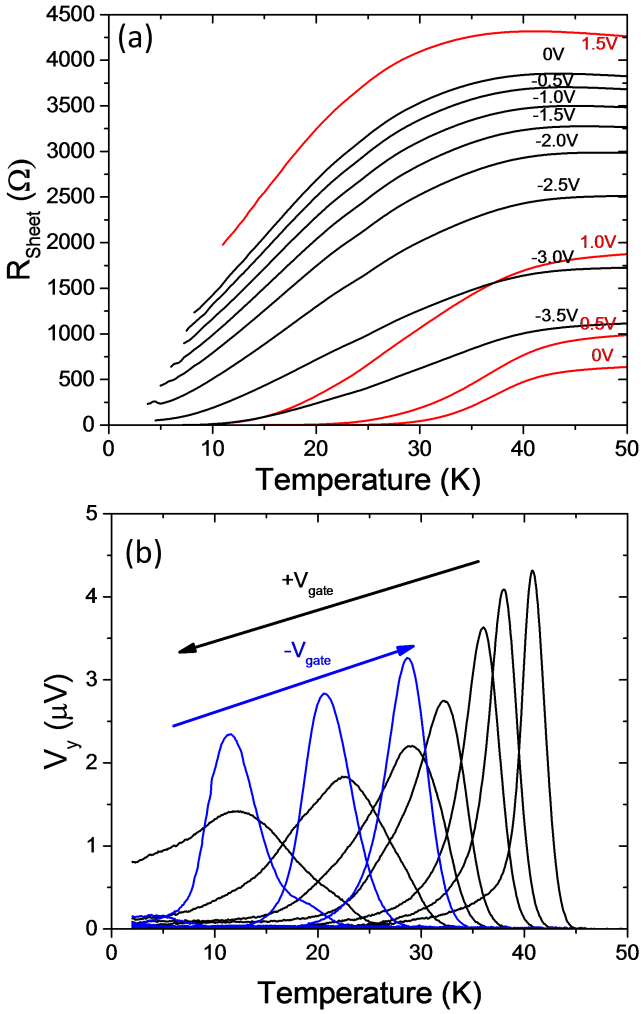

Figure 3.8: (a) Resistance vs temperature at a series of gate voltages for a 4 unit cell LCO film showing a clear hysteresis. (b) The imaginary component of the pickup coil voltage as outlined in Section 4.2 for a series of gate voltages in a 3 unit cell LCO film. We are plotting the pickup coil voltage for this sample instead of the resistance because the contacts failed before we had a chance to reverse the voltage. In both, the initial sample was near optimal doping and we first applied a positive gate voltage followed by a negative gate voltage.

Chapter 4

Measurement Techniques

Our goal is to understand the fundamental properties of superconducting materials and we have three primary probes in this regard. Two of these probes are connected to the two fundamental properties that are integral to all superconductors. Those properties are zero resistance and the Meissner effect. We are interested in probing both of these fundamental properties and use a combination of techniques. We use standard four-terminal transport measurements to measure the resistance of the sample as a function of temperature. We use a two-coil mutual inductance technique to probe the screening currents produced in the superconducting state. The idea is that measuring transport alone will tell us that a superconducting sample has zero resistance and nothing more. By probing the Meissner effect of the superconductor we can quantify the strength of the superconducting state, namely the density of superconducting electrons. We are also interested in how both of these properties change as we adjust the doping of our material using ionic liquids, and we will use the Hall effect to determine where we are in the doping phase diagram. Section 4.1 will cover the details of the resistance and Hall Effect measurements and Sec. 4.2 will go into detail on

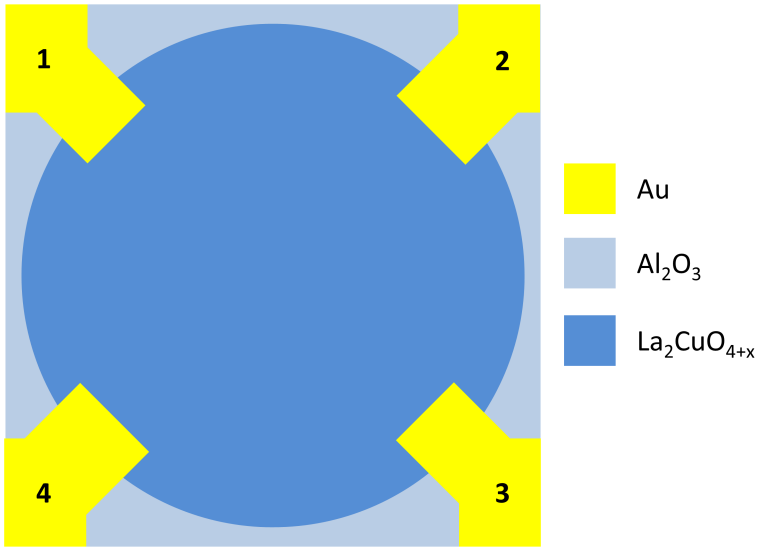

Figure 4.1: The typical layout for a superconducting La_2CuO_{4+x} sample. The gold electrodes are shown in yellow, the dark blue is the La_2CuO_{4+x} thin film and the light blue is Al_2O_3. The LCO film actually covers the Al_2O_3 region as well but due to the roughness created by the underlying Al_2O_3 film the La_2CuO_{4+x} does not grow epitaxially and is disordered and is nsulating in this region.

the two-coil mutual inductance technique we use for measuring the penetration depth.

4.1 Transport

We use a four terminal setup for measuring the transport properties of our La_2CuO_{4+x} (LCO) thin films. The sample and electrode pattern are shown in Fig. 4.1. The sample is patterned into a circular disk to produce a cylindrically symmetric shape for the two coil mutual inductance technique, which we will look at in more detail in Sec. 4.2. We pattern the sample by first depositing Al_2O_3 in the region where

we do not want superconducting LCO. We then deposit LCO on the entire sample surface but the regions where LCO is on top of Al_2O_3 do not grow epitaxially due to the rough surface and lattice mismatch created by the Al_2O_3 film and the film in these regions is disordered and insulating. The last step is to deposit gold electrodes in the four corners of the sample for measuring resistance. We use the procedure developed by L. J. van der Pauw [30] to determine the sheet resistance, R_s, of the film where

$$e^{-\pi R_{12,43}/R_s} + e^{-\pi R_{23,14}/R_s} = 1. \tag{4.1}$$

The numbering convention of the resistance measurements in Eqn. 4.1 refer to $R_{I^+I^-,V^+V^-}$, where the first pair of numbers refererence the current leads and the second pair reference the voltage leads. The numbering convention in Eqn. 4.1 is the same as in Fig. 4.1. In principle there is no problem with solving the above equation for every measured resistance, but in practice when $R_{12,43}$ and $R_{23,14}$ are within 20% of each other, which is true for the data presented in this thesis, and we can use the simplification of

$$R_s = \frac{\pi}{\ln(2)} \frac{R_{12,43} + R_{23,14}}{2}. \tag{4.2}$$

In addition to determining the sheet resistance we also want to measure the Hall Effect to find the doping of our film. For this we define the transverse resistance using

$$R_{xy} = \frac{R_{13,24} + R_{24,31}}{2}. \tag{4.3}$$

This combination of resistances cancels out the longitudinal component in each of the two measurements and leaves us with the bare transverse resistance. The transverse resistance allows us to determine both the type of the charge carrier in our material and the density of charge carriers. A sample data set of R_{xy} is

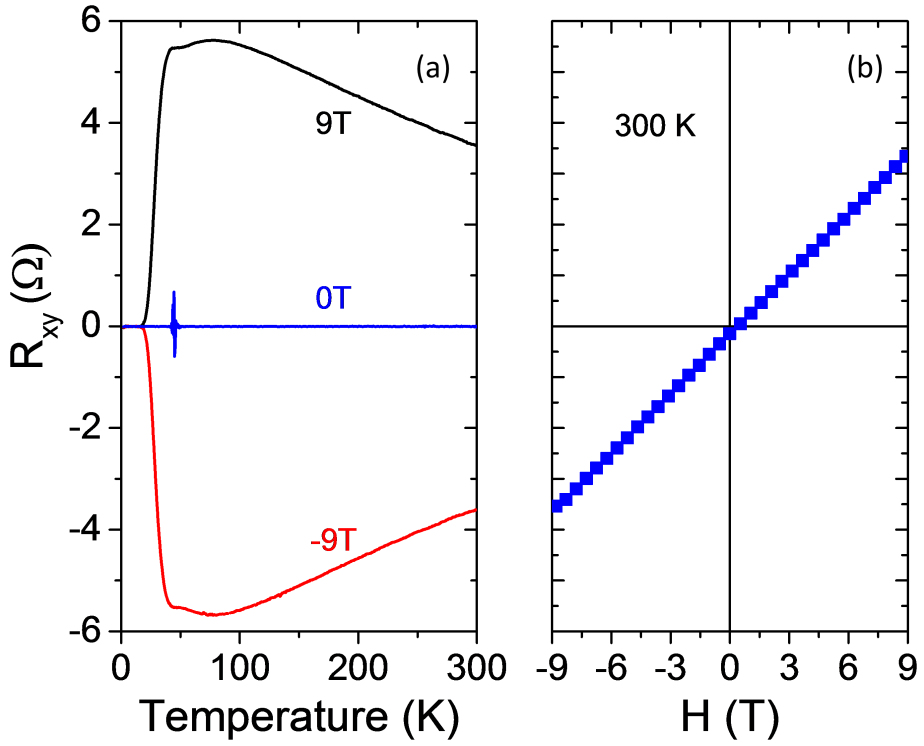

Figure 4.2: (a) R_{xy} vs temperature for a typical 4 unit cell La_2CuO_{4+x} film at 0, 9T, and -9T. The zero field case shows no signal demonstrating the combination of resistances from Eqn. 4.3 do in fact remove the longitudinal component of the resistance. The positive and negative field curves mirror each other about the x-axis implying the hall signal is symmetric We can also see that the signal is linear in (b), which is a sweep of the magnetic field taken at 300 K.

shown in Fig. 4.2 for a four unit cell LCO film. We see that the Hall signal is symmetric about zero and linear with magnetic field. We also see that as a function of temperature the transverse resistance goes though a maximum before diving to zero below T_c.

From the transverse resistance we calculate the 2D carrier concentration as $n_{2D} = \frac{B}{qR_{xy}}$ assuming a free electron gas model with only a single type of charge carrier, where B is the applied perpendicular magnetic field and q is the charge of an electron. We can also calculate the Hall mobility as $\mu_H = \frac{1}{qn_{2D}R_s}$, where R_s

is the sheet resistance found from Eqn. 4.2 . The van der Pauw formalism makes an assumption that our contacts are infinitely small. Because our contacts are in fact a significant fraction of the size of the sample we estimate an error of up to 20% in our calculations for sheet resistance and carrier concentration due to the finite size of our contacts [31] .

4.2 Two-Coil Mutual Inductance Technique

The two-coil mutual inductance measurement is a technique for probing the penetration depth or kinetic inductance of a material. Kinetic inductance and penetration depth are simply two different sides of the same coin. If we want to talk about penetration depth we are thinking about the length scale over which magnetic fields die away at the surface of a superconductor. This screening of magnetic fields is referred to as the Meissner effect and along with zero resistance makes up the two fundamental properties of a superconducting material. The other way we can think is in terms of kinetic inductance. The idea here is to picture the charge carriers within the conducting material. These charge carriers are moving and therefore have kinetic energy. This kinetic energy or momentum makes these carriers resist changes in the applied current, which on a macroscopic scale is the same as an inductance. Either picture, kinetic inductance or penetration depth, is equally good, and there is no standard within the literature. More importantly in the limit of a thin film ($\lambda > d$) they are directly related by

$$L_k = \frac{\mu_0 \lambda^2}{d}, \tag{4.4}$$

where L_k is the kinetic inductance, λ is the penetration depth, d is the thickness of the film and μ_0 is the permeability of free space[32].

The two-coil mutual inductance technique, as the name implies, makes use of a pair of coils. The first is a drive coil used to create an alternating magnetic field, which will induce screening currents in our superconducting sample. The second coil is a pickup coil which is used to sense the magnetic field produced by the screening currents of the sample. An early development of the two-coil technique was by Fiory and Hebard in 1980[33], where they showed evidence for a Berezinskii-Kosterlitz-Thouless transition in Al thin films. They also applied this technique to the high-T_c superconductor YBCO as early as 1988[34]. As early as 10 years ago there was working being done using a conventional gate and solid dielectric to adjust the doping and transition temperature in LSCO and track the corresponding changes in kinetic inductance[12]. We are specifically modeling our two coil setup on a design by Jeaneratte[35] and first implemented in our lab by Zhong-Heng Lin[36, 37]. The unique aspect of this design is that both the drive and pickup coils are on the same side of the sample. This is critical for our experiments involving ionic liquid because the top side of the sample is already occupied by the ionic liquid and gate.

We use the following numerical procedure for extracting the material property of penetration depth from the measured quantities of the real and imaginary components of the pick-up coil voltage. Our goal is to develop a procedure where we can input voltages, which are our measured quantity, and output the penetration depth, which is the material property we are interested in. It turns out this is a much simpler problem to work in reverse and our strategy will be to initially work the problem starting from the penetration depth and determining the corresponding measured voltages. The strategy will be to first develop a procedure for inputing the material properties of resistance and penetration depth, which we will represent as a complex film impedance. We will use this input complex

film impedance to calculate the voltage produced in our pickup coil. The second step will be to develop an efficient guess and check procedure for inverting this process to convert the actual measured voltages into the material properties.

Our first goal will be to derive the steps needed to calculate the measured voltages from the input complex film impedance. There will be two main steps in this derivation. First we divide the sample into a series of rings, derive a linear system of equations, which we use to solve for the current in each ring. Once we have determined the currents in the film we then derive the magnetic field produced by these currents and the corresponding voltages produced in the pickup coil due to these currents.

We begin with a statement of Ohm's law in the form

$$\mathbf{J} = \sigma \mathbf{E} = -i\omega\sigma \mathbf{A}, \tag{4.5}$$

where σ is the complex conductivity of the material and we have assumed that all fields have a time dependence of the form $\exp(i\omega t)$. In general, the conductivity is a complex quantity with both real and imaginary components. Going forward we will rewrite the conductivity in terms of a complex impedance, Z, as

$$\frac{d}{\sigma} = Z = R_s + i\omega L_K, \tag{4.6}$$

where R_s is the sheet resistance and L_K is the kinetic inductance defined in Eqn. 4.4. R_s is the same as the sheet resistance defined in Eqn. 4.2, which we will measure using a four-terminal DC technique, and the two coil will provide us with an independent measurement of this same quantity.

We define the vector potential in general as

$$\mathbf{A}(\mathbf{r}) = \frac{\mu_0}{4\pi} \int \frac{\mathbf{J}(\mathbf{x}')}{|\mathbf{x} - \mathbf{x}'|} \, \mathrm{d}^3 x'. \tag{4.7}$$

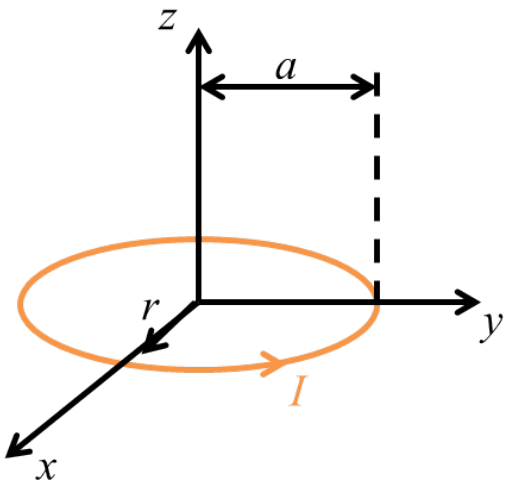

Figure 4.3: The current loop and coordinates we use for defining the vector potential produced by a loop of current in Eqn. 4.8. The circle shown in orange is the current loop of radius a. Due to the cylindrical symmetry of the setup, we define the vector potential using the coordinates r and z.

Our film is patterned into a disk, which we will numerically treat as a series of concentric rings, and both coils are arranged to maintain cylindrical symmetry with the sample disk. This means the relevant vector potential we will need to calculate is that of a ring which we can take from Jackson[38]. Using the coordinate definition shown in Fig. 4.3 with the loop to be in the xy plane there is only a phi component for the vector potential expressed as

$$A_\phi(r,z,a) = \frac{\mu_0}{4\pi}\frac{4Ia}{\sqrt{a^2+r^2++z^2+2ar}}\left[\frac{(2-k^2)K(k)-2E(k)}{k^2}\right], \tag{4.8}$$

where $K(k)$ and $E(k)$ are elliptic integrals whose argument k is defined as

$$k^2 = \frac{4ar\sin\theta}{a^2+r^2+z^2+2ar}. \tag{4.9}$$

We combine Eqn. 4.5 and Eqn. 4.6 as

$$\frac{\mathbf{J}dZ}{i\omega} = \mathbf{A}_{drive} + \mathbf{A}_{film}, \tag{4.10}$$

where we have broken the vector potential into two components originating from the drive coil and the screening currents in the film.

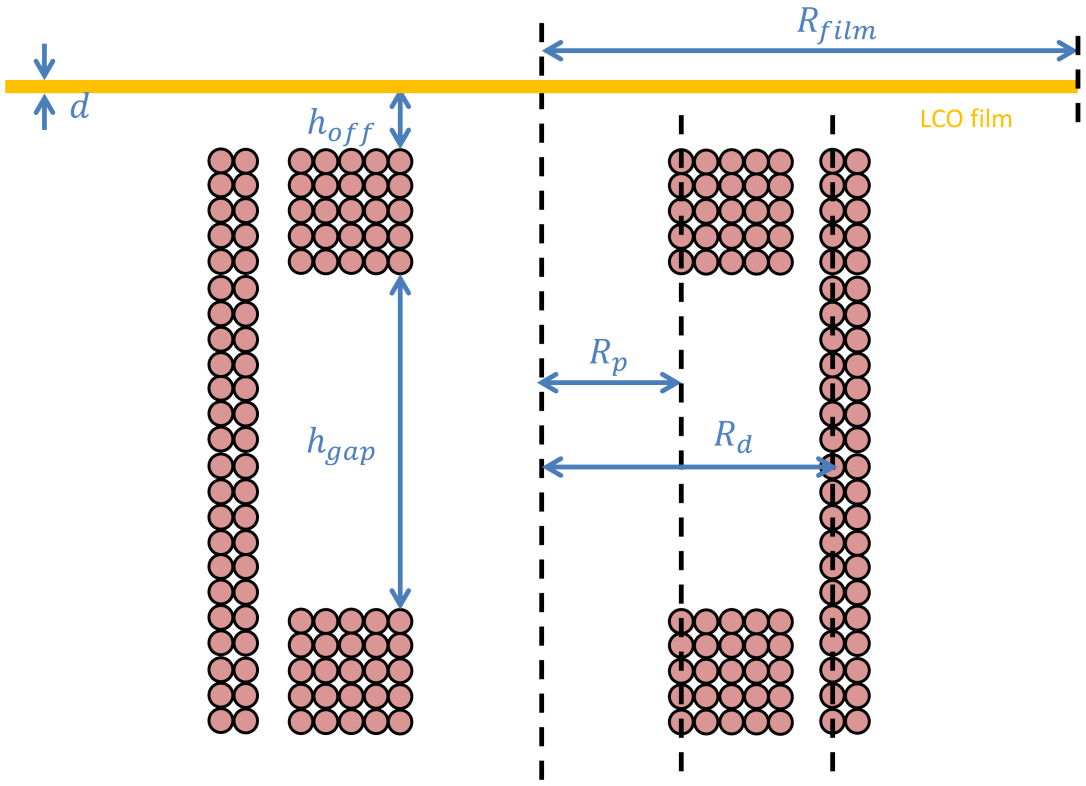

Figure 4.4: The geometric layout of the drive and pickup coils. Tab. 4.1 details the exact measurements for the two coil used in this work. The pickup coil is wound in two parts with the part near the sample wound in one sense and a part far from the sample wound in the opposite sense in order to minimize the direct coupling between the drive and pickup coil.

We write Eqn. 4.10 in a more explicit form using the exact geometry of our coils shown in Fig. 4.4 and Tab. 4.1. With this information we build a linear set

R_d	1.5 mm
δ_d	0.1 mm
L_d	2
T_d	23
R_p	1 mm
δ_p	0.1 mm
L_p	5
T_p	5
h_{gap}	1.4 mm
h_{off}	0.67 mm
N_{rings}	100
R_{film}	2.5 mm
d	40 Å
I_d	1 mA

Table 4.1: The geometric properties of the two coil setup used for determining the penetration depth of superconducting thin films. The subscript d refers to the properties of the drive coil and the subscript p refers to properties of the pickup coil. The diameter of the wire is δ, L is the number of layers in a coil, and T is the number of turns per layer. For the pickup coil L_p and T_p are the values for each of the oppositely wound pairs.

equations, one equation for each ring of current in the film, as

$$\frac{J_i dZ}{i\omega} = \sum_{l=0}^{L_d} \sum_{t=1}^{T_d} I_d A_\phi(\delta_d(t-1), r_i, R_d + \delta_d l) - \sum_{j=1}^{N_{rings}} J_j d\Delta r A_{ij}. \tag{4.11}$$

The drive coil component requires a sum over each loop of the drive coil, which takes the form of a pair of sums, one over the loops in each layer of the drive coil and one over the number of loops in the drive coil. The film component is a summation over each ring of current in the film. Care needs to be taken when we consider the A_{ii} term, which is the vector potential produced by a ring of current in the film on itself. We follow the work outlined in Z. H. Lin's thesis [36], which

solves for this term as

$$A_{ii} = I_i \frac{\mu_0}{2\pi} \left(\ln \left[\frac{16 r_i}{\Delta r_i} \right] + \left(\frac{\Delta r_i}{12 r_i} \right)^2 + \frac{1}{3} \left(\frac{\Delta r_i}{8 r_i} \right)^2 \ln \left[\frac{16 r_i}{\Delta r_i} \right] \right). \tag{4.12}$$

The only unknowns in Eqn. 4.11 are the current in the film, J_i, and the complex impedance of the film, Z. By making a guess for the impedance, we then have all the information needed to solve for the current in the film. An example of such a solution is shown in Fig. 4.5 using a the geometric values listed in Tab 4.1 and a penetration depth of 3700 Å, where we have assumed R_s is zero and used Eqn. 4.4 and Eqn. 4.6. For reference the critical current in YBCO can exceed 10^9 A/m^2 [39] and the current we calculate are approximately 100 times less than that value.

The next step is to go from the calculated screening currents in the film to the measured voltage in the pickup coil. We begin with a definition of mutual inductance as

$$V_p(emf) = -M \frac{dI_d}{dt} = -i\omega I_d M, \tag{4.13}$$

where once again we have made the assumption that the driving current have a time dependence of the form $\exp(i\omega t)$ and the mutual inductance can be defined as

$$M_{ij} = \frac{1}{I_j} \oint \mathbf{A_{ij}} \cdot d\mathbf{l}. \tag{4.14}$$

Using the specific geometry outlined in Fig. 4.4 and Tab. 4.1 we rewrite

$$\begin{aligned} M = & \frac{2\pi}{I_d} \sum_{l=0}^{L_p} (R_p + \delta_p l) \sum_{t=1}^{T_p} \sum_{i=1}^{N_{rings}} J_i \Delta r dA_\phi (\delta_p (t-1), R_p + \delta_p l, r_i) \\ & - \frac{2\pi}{I_d} \sum_{l=0}^{L_p} (R_p + \delta_p l) \sum_{t=1}^{T_p} \sum_{i=1}^{N_{rings}} J_i \Delta r dA_\phi (\delta_p (t-1) + h_{gap}, R_p + \delta_p l, r_i) \end{aligned} \tag{4.15}$$

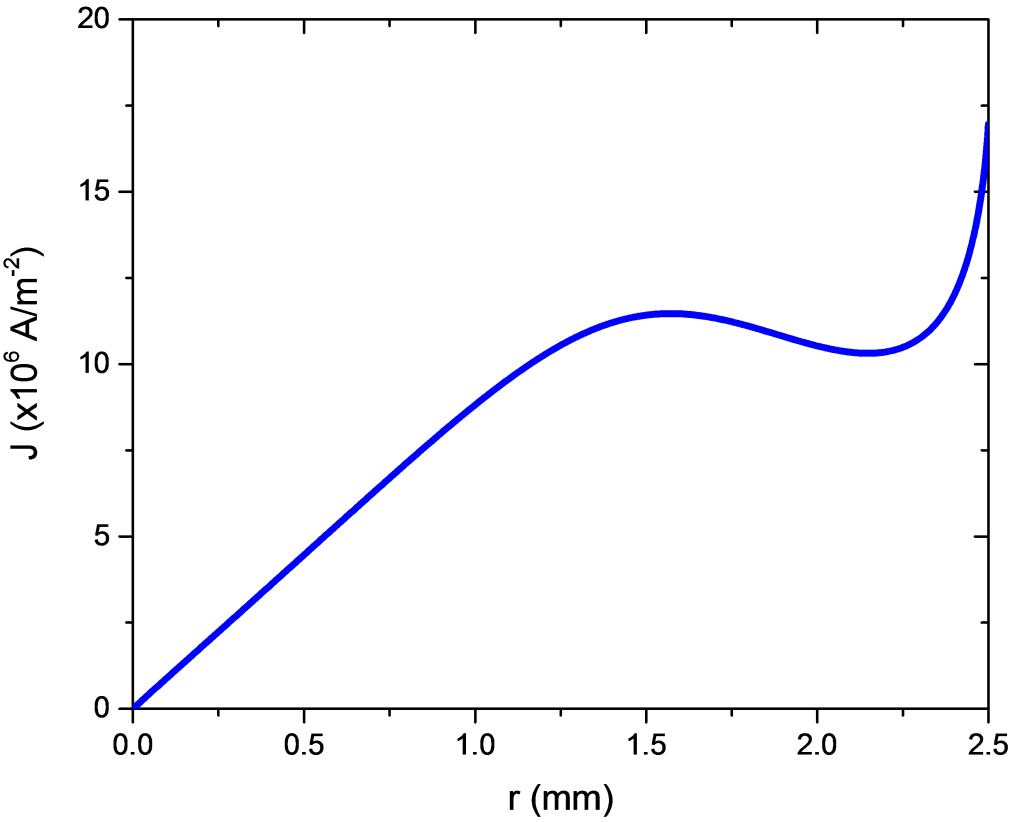

Figure 4.5: The calculated current density of a 3 unit cell La_2CuO_{4+x} film with a 5 mm diameter. We see the currents in the film reaches a local maximum at 1.5 mm, which corresponds to the radius of the drive coil, and peaks at the edge of the film.

The combination of Eqns. 4.11, 4.13, and 4.15 provide a function for inputting a guessed complex film impedance and calculating the resulting voltage in the pickup coil. In practice we measure the voltages in the pickup coil and wish to determine the corresponding film impedance. Our next goal is to determine how to invert this data.

The inversion procedure, taking the measured voltage and calculating the penetration depth and sheet resistance, follows a guess and check strategy. There are

two primary forms this strategy can take in order to invert the data. One involves building a large table of all the possible values we expect to encounter in a given experiment and then use that table to process each sweep. The second strategy we have employed is to take each data point one at a time and search out a matching set of voltages. The first strategy requires both more time up front and detailed knowledge of exactly what the parameter space of the data will be. The time element is approximately 12-24 hours to build a single table. This is a reasonable amount of time for creating a table that will then be used invert several days to weeks of data. However, if our initial estimate on what parameter space this table needs to cover is wrong or if a calibration factor changes we need to rebuild this table and spend another 12-24 hours. The alternative approach that in a big picture sense is less efficient is to a each data point one at a time. It is less efficient in the fact that we will sometimes recalculate the same voltage combinations we covered previously because we are treating each data point as a separate problem that does not inform the next data point. The advantage of the point by point inversion is it will adapt specifically to the data and does not require any prior prediction of what parameter space will need to be covered. The time cost is about 1 hour per data sweep, which means if you are processing less than 10-20 curves it is actually faster than the alternative method where one builds a giant table.

In detail the point by point guess and check inversion procedure involves a function that is made up of two main components. One component minimizes the error in the overall magnitude of the complex measured voltage by adjusting the guessed penetration depth. The other component minimizes the error in the ratio of the real to the imaginary component of the voltage by adjusting the guess in the sheet resistance. The magnitude of the adjustment scales with the magnitude of

the error and these two components cycle back and forth until the error between the calculated voltages and the measured voltages is smaller than the noise level of the measurement, which is 10 nV.

For the two coil measurement we use an SRS830 lock in amplifier in conjunction with an SRS 560 filter and amplifier to both apply and measure the two coil signals. The typical drive coil current is 1mA, which produces a magnetic field of approximately 15 mOe at the center of our sample. The drive frequency for our measurements is 50 kHz. A typical set of voltage measurements as well as the corresponding components of the film impedance are shown in Fig. 4.6. We first subtract off a zero signal which we measure by performing the same temperature sweep without the sample. This background subtraction removes the direct coupling between the drive coil and pickup coil. The coil is designed to minimize this direct coupling by winding the pickup coil in two components each wound in an opposite sense. The signal we are interested in is only the coupling though the superconducting film. Due to imprecise knowledge of the distance between the coils and the sample, we cannot determine the absolute size of the penetration depth. For example, an error of 0.05 mm in the distance h_{off} would correspond to a 40% error in the calculated penetration depth. Instead, to set the scale, we use 2700 Å based on literature values for $La_{2-x}Sr_xCuO_4$[40, 41, 42] a compound with a similar transition temperature, to calibrate the unknown spacing between the sample and the coils. This calibration is used with the optimally doped sample and then subsequent measurements after changing the doping using ionic liquids can be determined relative to this initial state. We are plotting the penetration depth as λ^{-2} because this quantity is proportional to the superconducting electron density. We can see that below T_c, which we define using the peak in V_x, the superconducting electron density steadily grows and the sheet resistance goes to zero. A check

of our measurement comes from comparing the sheet resistance measured by the two coil and the sheet resistance measure by the DC van der Pauw procedure. We see good agreement between these two measurements, which is a confirmation that our numerical procedure for determining the film impedance from the two coil signal is behaving as expected.

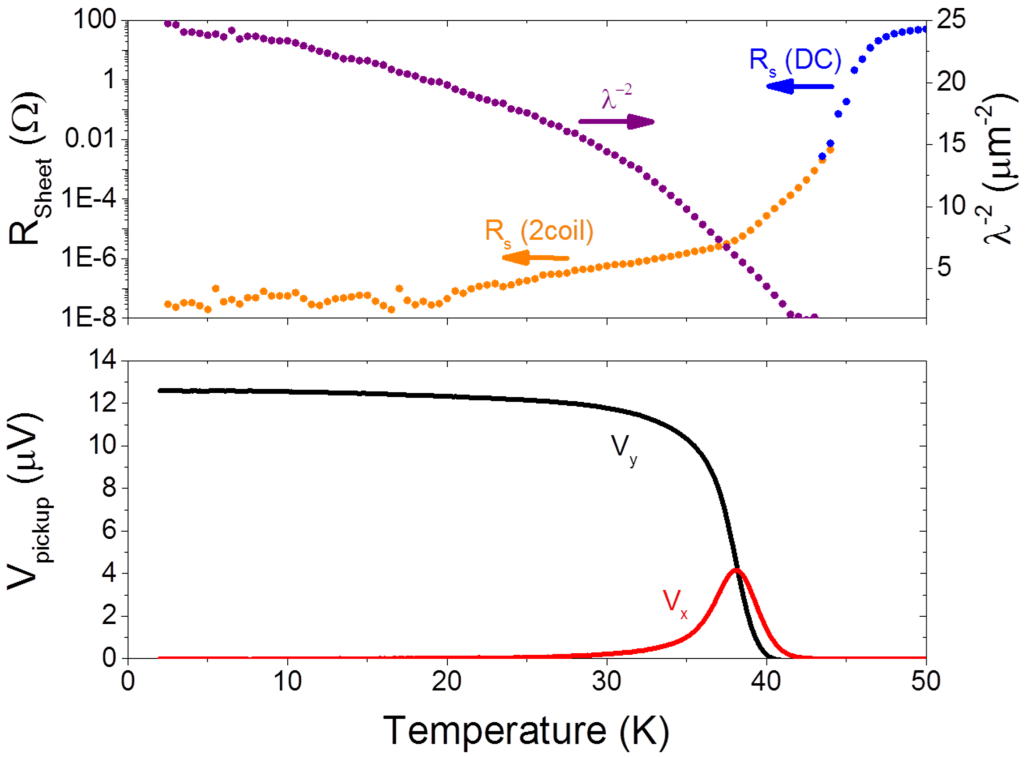

Figure 4.6: (top) the real and imaginary components of the resistance of a superconducting La_2CuO_{4+x} film expressed as the sheet resistance and λ^{-2}. The blue data points are the sheet resistance measured using a standard 4 probe DC technique and we see that it overlaps with the resistance determined from the two-coil resistance. (bottom) The real and imaginary parts of the measured voltage in the pickup coil used to calculate the film properties plotted above.

There are three primary material properties that we wish to measure in the

superconducting films under study in this thesis. We want to measure the sheet resistance, the Hall Effect, and the penetration depth. We use a four terminal van der Pauw configuration for measuring both the sheet resistance and the Hall Effect. From the Hall Effect we calculate the carrier concentration and mobility of this film, both of which inform our understanding of how exactly ionic liquid is affecting the film. We use a two-coil mutual inductance technique for measuring the penetration depth of the films. The penetration depth provides insight into the superconducting electrons in the film telling us about the strength of the superconducting state. By explicitly measuring all of these variables we will be able to explore the interplay and fundamental relationships underlying the superconducting state with a minimal need for assumptions about where we are in the superconducting phase diagram.

Chapter 5

Results and Discussion

The previous chapters outlined all the tools we need to thoroughly explore the doping phase diagrams of superconducting films. In this chapter we will put these tools to use and see how the resistance, T_c, doping, and penetration depth are all interconnected. There are a number of empirical relationships about how T_c is fundamentally connected to the penetration depth in a superconductor and our experimental setup is uniquely designed to test these empirical relationships. We will see that the scaling relationship of $\lambda(0)^{-2} \propto \sigma T_c$ established by Homes *et al.* [4, 5, 43] is upheld in our samples, and we present a simple explanation for this scaling based on the fact that scattering is strong in these films. We also explore the proposal established by Uemura *et al.* [44] of $\lambda(0)^{-2} \propto T_c$and find that our results do not support this empirical relationship. In fact, a central result of our measurements is that the superconducting electron density is proportional to the carrier concentration in the normal state of the material. A consequence of this proportionality is that instead of observing the Uemura relationship, we find a remapping of the superconducting dome. Section 5.1 will detail the experimental

setup and how using ionic liquid to adjust the doping drives changes in the resistance, T_c and the penetration depth. We look closely at the low temperature dependence of the penetration depth in Sec. 5.2, which will inform our understanding of the pairing state in these films. Finally, Sec. 5.3 and 5.4 will cover the degree to which our results agree with the empirical relationships established by Homes and Uemura, respectively.

5.1 Dependence on Carrier Concentration

The experimental setup is shown in Fig. 5.1. Both the drive and pickup coils are located on the back side of the sample. The holder is constructed out of Delrin in order to minimize stray coupling between the drive and the pickup coil. We use the numerical procedure outlined in Sec. 4.2 for determining the penetration depth of the sample from the measured real and imaginary components of the voltage read by the pickup coil. We model the film with a complex impedance, $Z = R + i\omega L_k$, where R and L_k are the sheet resistance and the kinetic inductance of the film, respectively. In the case of a thin film with thickness $\lambda \gg d$, the kinetic inductance is directly related to the London penetration depth as $L_k = \mu_0 \lambda^2 / d$.

We used the ionic liquid DEME-TFSI to tune the properties of our superconducting samples. The ionic liquid is initially applied to the surface of the sample at room temperature but all further gating is done at 245 K. Figure 5.2 shows how the resistance, carrier concentration, and mobility evolve with the applied gate voltage at a temperature of 180 K. All three quantities were determined using the four-wire resistance technique in a Van der Pauw configuration as outlined in Sec. 4.1. Each measurement step involves warming the sample and ionic liquid to 245 K, which is above the melting point of the liquid. The gate voltage is then

changed at this elevated temperature and allowed to relax for 20 min. We apply a positive voltage to the gate, which corresponds to removing holes or reducing the number of charge carriers in the sample. As the gate voltage is increased we see both an increase in the resistance of the film and a decrease in the carrier concentration. While the mobility does begin to decrease at higher gate voltages we see that the primary effect of the applied voltage is to reduce the number of free holes in the material. We note that the gating procedure is not purely electrostatic as the changes upon gating are irreversible. The evidence for this conclusion comes from removing the applied gate voltage and observing that the resistance does not return to the zero-voltage state. In fact, we must apply a negative gate voltage in order to return the resistance to its initial state. Now, while there are advantages to a purely electrostatic process, namely reversibility and no introduction of disorder, an *in-situ* electrochemical doping method, which we believe may be involved in the process presented here, is still a powerful and useful tool.

The real and imaginary components of the voltage in the pickup coil at a series of applied gate voltages are shown in Fig. 5.3. The real component has a peak centered at the superconducting transition and the width of the peak is, in part, a measure of the homogeneity of the sample at that doping. We see that with increasing applied gate voltage the peak moves to lower temperatures and broadens. We interpret this as a change in the doping of the material, removing holes, but not necessarily in a fully homogeneous way. We will use the center of this peak as our definition of T_c for the purposes of checking the Homes scaling relation. The imaginary component of the voltage, while not explicitly equal to it, represents the kinetic inductance of the sample which is directly related to both the penetration depth and superconducting electron density. We see the

imaginary component move to lower temperatures and go to zero with increasing gate voltage.

We follow the inversion procedure outlined in Sec. 4.2 to convert from the measured voltage to the penetration depth. Fig. 5.4 shows the results of this conversion, where we are plotting the quantity λ^{-2}, which is proportional to the superconducting electron density ρ_s. The measurement of the resistance of the sample obtained in parallel with the two-coil signal is shown in Fig.5.5. We see that as we increase the gate voltage and remove holes the normal state resistance increases and T_c steadily decreases.

A summary of the results is shown in Fig. 5.6. The range in doping covered here is from the underdoped edge of the superconducting dome to near the peak of the dome. We can convert from 2D carriers/cm^2 to holes/Cu using the fact that there are six CuO_2 planes in a three unit cell LCO film. Given this conversion we cover a range of 0.07 to 0.21 holes/Cu, which is in agreement with the generally accepted phase diagrams for high-T_c superconductors. The conductivity roughly follows a Drude form, where the conductivity is proportional to the carrier concentration. The quantity λ^{-2}, which is proportional to the superconducting electron density, ρ_s, also increases directly proportional to the normal state carrier concentrations. This means that the number of electrons that collapse into the superconducting state is proportional to the number of electrons in the normal state. While the superconducting electrons must be a subset of the normal state electrons, this result showing that these quantities are explicitly proportional is new and a product of our unique experimental setup that allows us to track both of these quantities in parallel.

Following the work of Zuev *et al.*[45] we can use the relationship

$$k_B T_{2D} = \frac{\Phi_0^2}{8\pi\mu_0} \frac{d}{\lambda^2(T_{2D})}, \tag{5.1}$$

to define T_{2D}, which is the Berezinskii-Kosterlitz-Thouless-transition temperature. Here Φ_0 is the flux quantum. If we use the entire film thickness of 40 Å as the value of d we find good agreement between this definition of T_{2D} and the value of T_c we determine from the peak of the real component of the two coil signal. The dashed line in Fig. 5.4 is a plot of Eqn. 5.1 assuming d is 40 Å and the temperature at where this dashed line crosses the $\lambda^{-2}(T)$ curve defines T_{2D}.

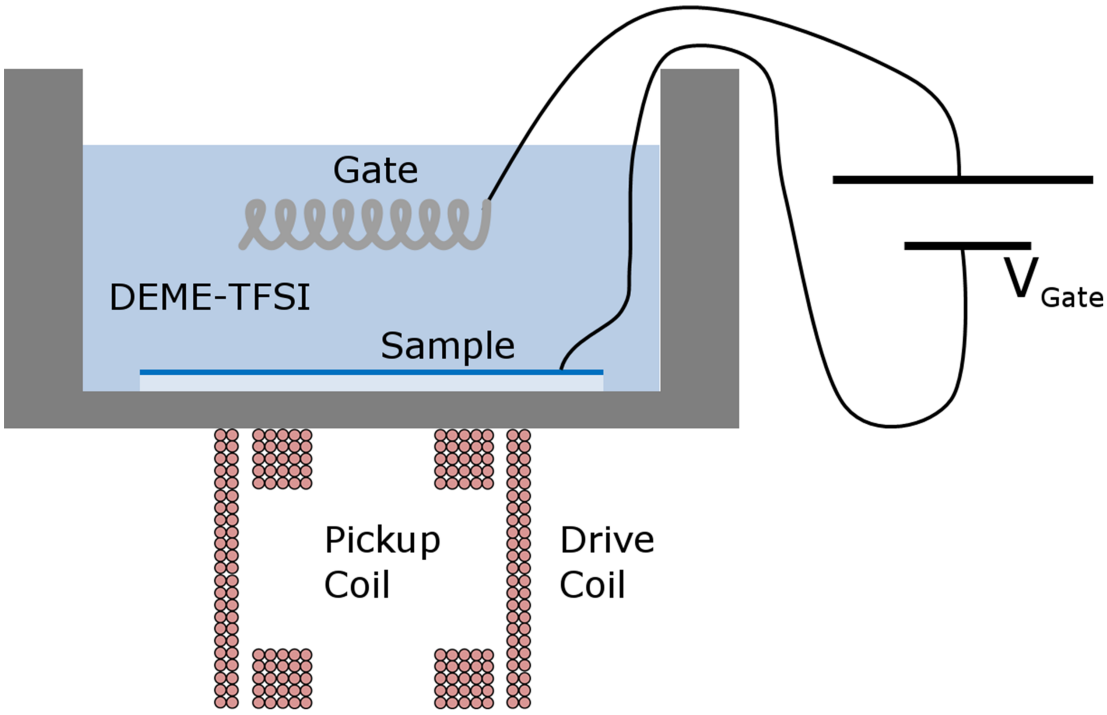

Figure 5.1: Schematic of the sample setup. The entire sample is immersed in the ionic liquid DEME-TFSI. A gate electrode made of Pt is also immersed in the ionic liquid. Not pictured are leads going to the corners of the sample for making resistance measurements. The sample holder is made of plastic (Delrin) to minimize extraneous screening currents. The two-coil assembly is composed of an outer drive coil and and inner pickup coil. The inner pickup coil consists of two oppositely wound sections to minimize the direct mutual inductance between the drive coil and the pickup coil. The sample is patterned into a disk with a 5 mm diameter. The inner diameters of the pickup coil and drive coil are 2 mm and 3 mm respectively. The gate is a coil of Pt wire with a surface area double that of the sample.

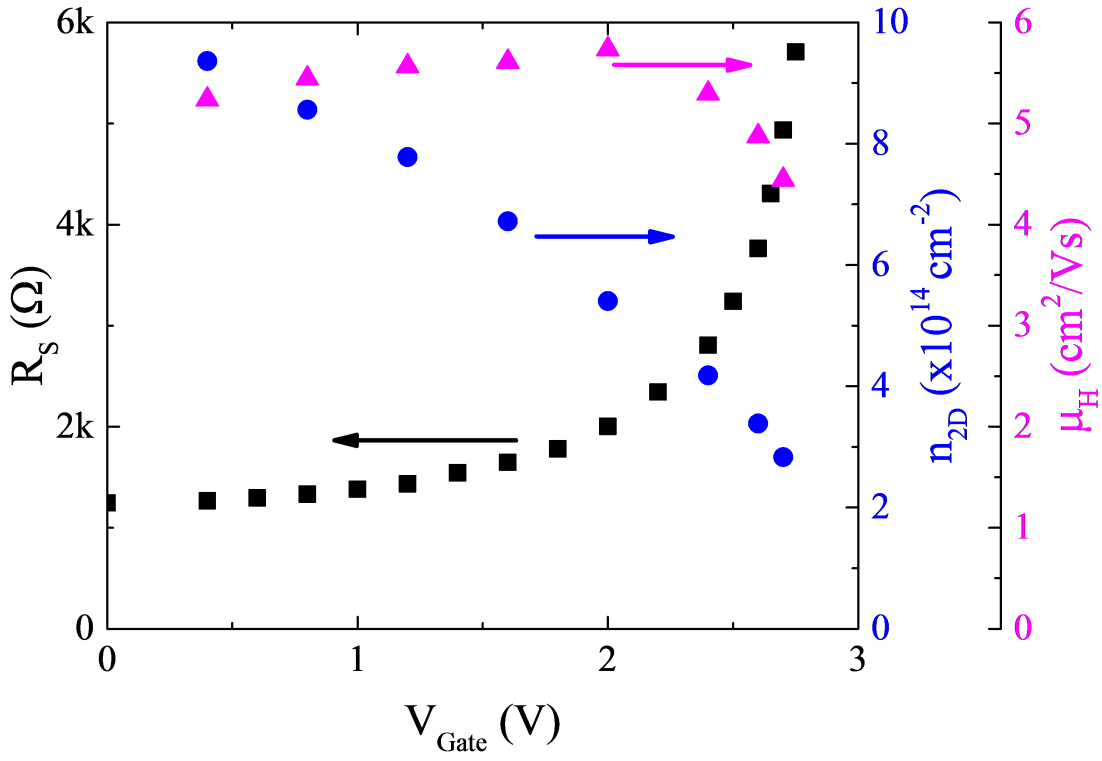

Figure 5.2: Plot showing how R_S(squares), n_{2D}(circles), and μ_H(triangles) evolve as the gate voltage is increased. All three quantities were measured at 180 K. We see that as we increase the gate voltage the resistance steadily increases and the number of free carriers decreases. We also note that, while the mobility does begin to decrease above 2.5 V, we are primarily affecting the carrier concentration of the film and for the most part the mobility remains constant.

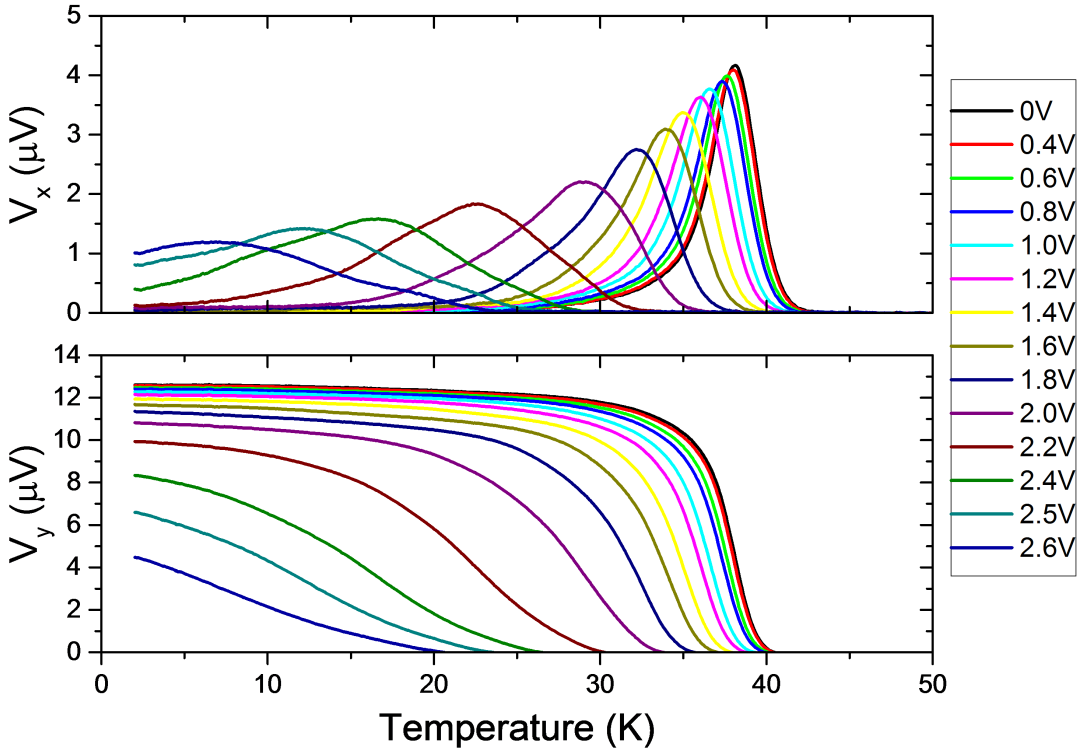

Figure 5.3: The real and imaginary components of the 2 coil signal showing how both evolve as a function of applied gate voltage.

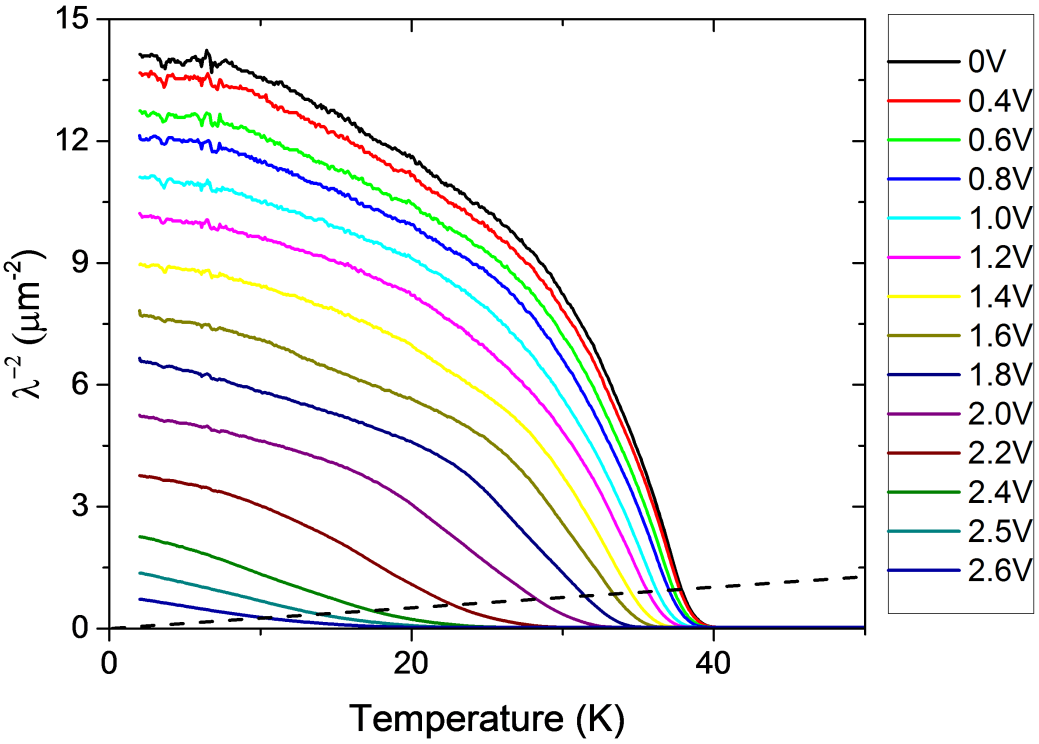

Figure 5.4: λ^{-2} vs Temperature for a range of applied gate voltages obtained from using the numerical procedure oulined in Sec. 4.2 to invert the real and imaginary components of the voltages in the pickup coil shown in Fig. 5.3. The dashed line is an estimate for the BKT transtion temperature assuming the entire film thickness is acting as a two dimensional unit.

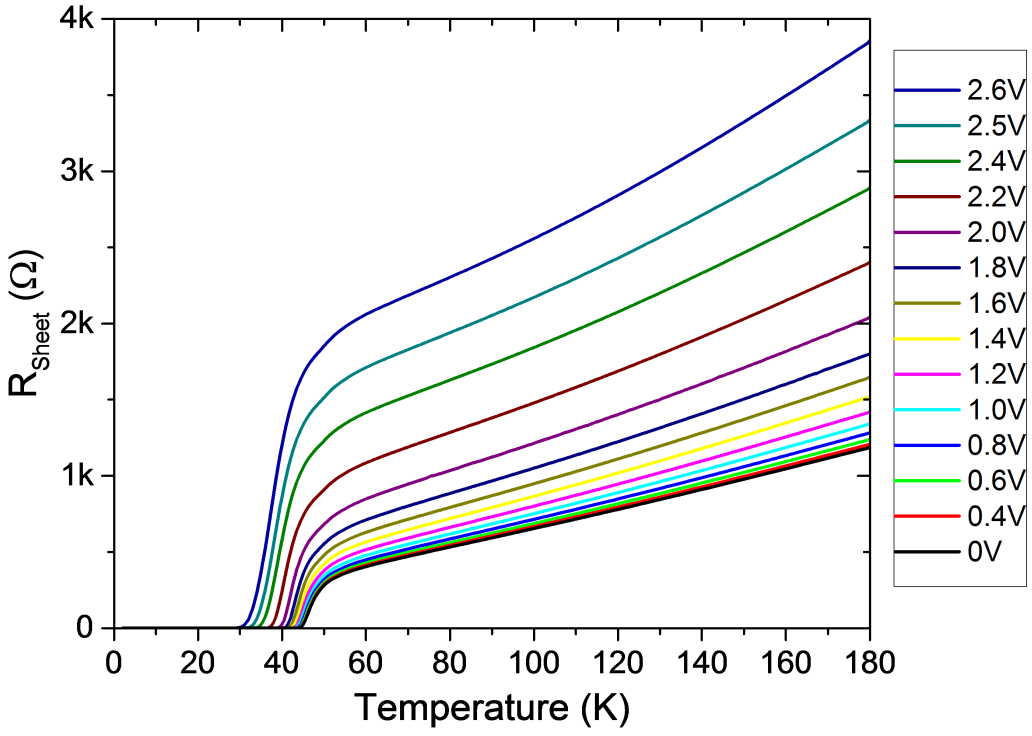

Figure 5.5: The sheet resistance vs temperature for a 3 unit cell La_2CuO_{4+x} film at a range of applied gate voltages. We see that as the gate voltage is increased the normal state resistance increases and T_c decreases.

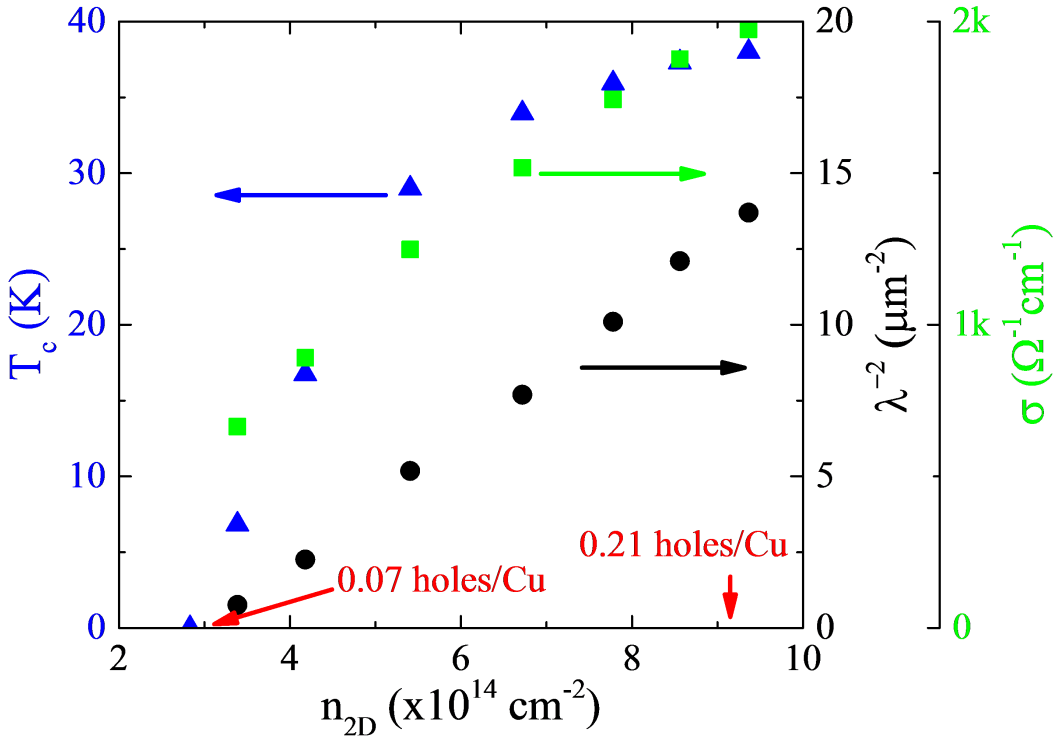

Figure 5.6: Plot showing how T_c(triangles), λ^{-2}(circles), and σ(squares) evolve as a function of doping in a 3 unit cell LCO thin film. For reference we include markers at the top and the underdoped edge of the superconducting dome, where the conversion from charges per square cm to holes per copper is done using the fact that we have a 3 unit cell sample which corresponds to 6 copper oxygen planes.

5.2 Low Temperature Dependance of Pentration Depth

There is important information about the pairing state of the superconductor contained in the low temperature dependence of the penetration depth. Depending on the pairing state of the superconductor we expect $\lambda(T)^{-2}$ to have a specific temperature dependence. For an s-wave pairing state with a full gap we expect an exponential dependence for $\lambda(T)^{-2}$. For a d-wave pairing state, where there are nodes in the gap, we expect a linear dependence for $\lambda(T)^{-2}$ [46]. In the case of strong scattering this linear dependence shifts to $\lambda(T)^{-2} \propto T^2$ [47, 48, 49, 50, 51]. Figure 5.7 shows that this sample exhibits a quadratic temperature dependence, which implies scattering is playing a significant role. The ultra thin nature of this sample means that the upper and lower surface roughness make up a large fraction of the thickness of the entire film. We used both X-ray reflectivity (XRR) and atomic force microscopy (AFM) to characterize the film roughness. From XRR our estimates of the substrate-sample interface roughness and the sample surface roughness are 3 Å and 8 Å, respectively. Using AFM we measure the sample surface roughness to be 3 Å. All of these quantities are significant compared to the c-axis lattice parameter, which is 13.3 Å. Considering that the entire film thickness is 3 unit cells and the roughness of both of the top and bottom surface are significant fractions of a unit cell it is reasonable to expect this film to be in the strong scattering limit.

We are interested in the value of the penetration depth at absolute zero, but our measurement is limited to a minimum temperature of 2 K. We will use the assumption that these film are in the dirty limit, based of the results in Fig. 5.7, to find the zero temperature penetration depth, $\lambda(0)$, by fitting the low temperature

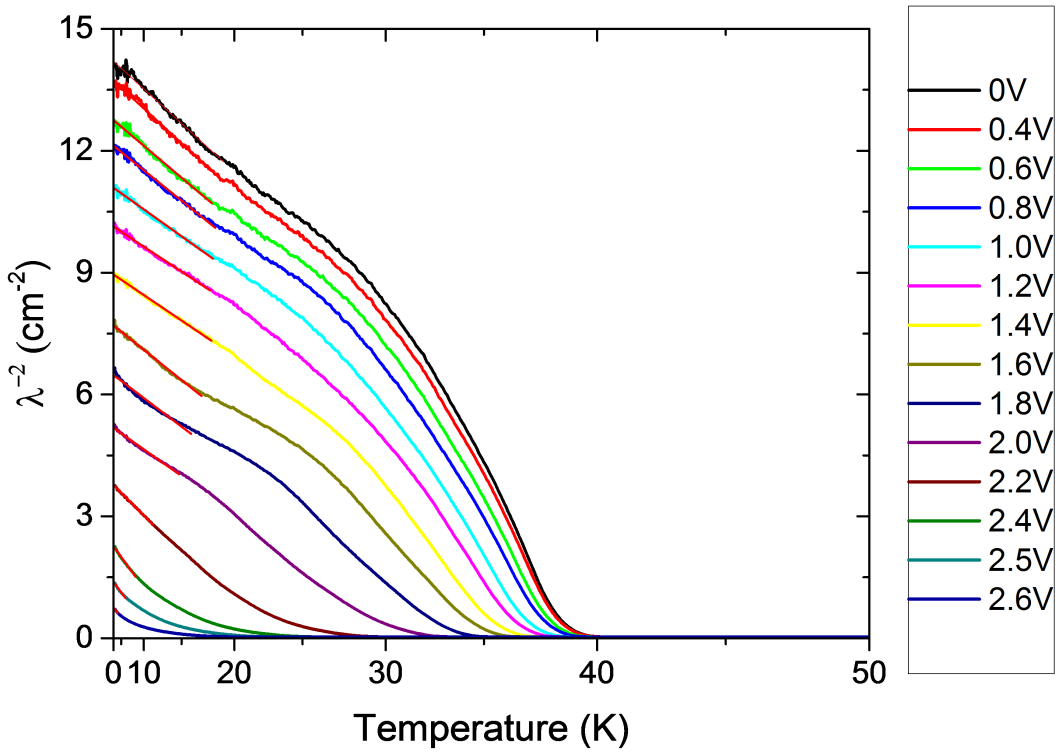

Figure 5.7: . $\lambda(T)^{-2}$ plotted on a T^2axis to emphasize the quadradic dependance at low temperature in agreement with this film being a d-wave superconductor in the strong scattering limit. The red lines are linear fits to the data from T=2 K to T= $T_c/2$ where the y-intercept of the fit is used to determine $\lambda(0)^{-2}$.

penetration depth data using the form

$$\lambda(0)^{-2} - \lambda(T)^{-2} \propto T^2. \tag{5.2}$$

We plot $\lambda^{-2}(T)$ vs T^2 and then use a linear fit to the data where $T < T_c/2$ to extrapolate to the zero temperature value. This extrapolated value is what we will use in our analysis of the Homes and Uemura scaling relationships in Sec. 5.3 and 5.4.

5.3 Homes Scaling

A primary conclusion of this thesis is that for ionic liquid gated LCO thin films we observe $\rho_s \propto T_c\sigma_{DC}$ in agreement with the results obtained for a wide variety of superconducting samples by Homes *et al.* [4, 5, 43]. Where the previous work required a massive collection of distinct samples, we are able to cover a similar range of parameter space in a single film continuously doped using ionic liquids. The convenience of this setup is one obvious advantage. Another advantage is that any uncertainty in the geometry of the sample is fixed. Because we are examining changes in the quantities of interest, small uncertainties in the absolute values do not effect the conclusions we draw here.

There are a number of different proposals for the interpretation of the $\lambda(0)^{-2} \propto \sigma T_c$ relationship [52, 53, 54, 55]. The simplest argument comes from the fact that the film is in the strong scattering limit ($\Delta \ll h\tau^{-1}$) to begin with. For our films we use a simple Drude model to estimate the scattering rate. Taking the values of R_s and n_{2D} from Fig. 5.2 and the relationship $\frac{1}{R_s} = \frac{n_{2D}e^2\tau}{m}$ we can calculate $h\tau^{-1}$ to be 1.3 eV, which is much larger than the superconducting gap in these types of materials [56, 57, 58]. This comparison is important because we can make a simple argument for why the Homes scaling relationship should hold in this limit. If we continue to assume a Drude model for the conductivity of our film, in the normal state the frequency dependence goes as

$$\sigma(\omega) = \frac{ne^2}{m}\frac{\tau}{1+\omega^2\tau^2}. \tag{5.3}$$

The energy range over which the conductivity is approximately constant is set by the scattering rate. When the sample transitions into the superconducting state

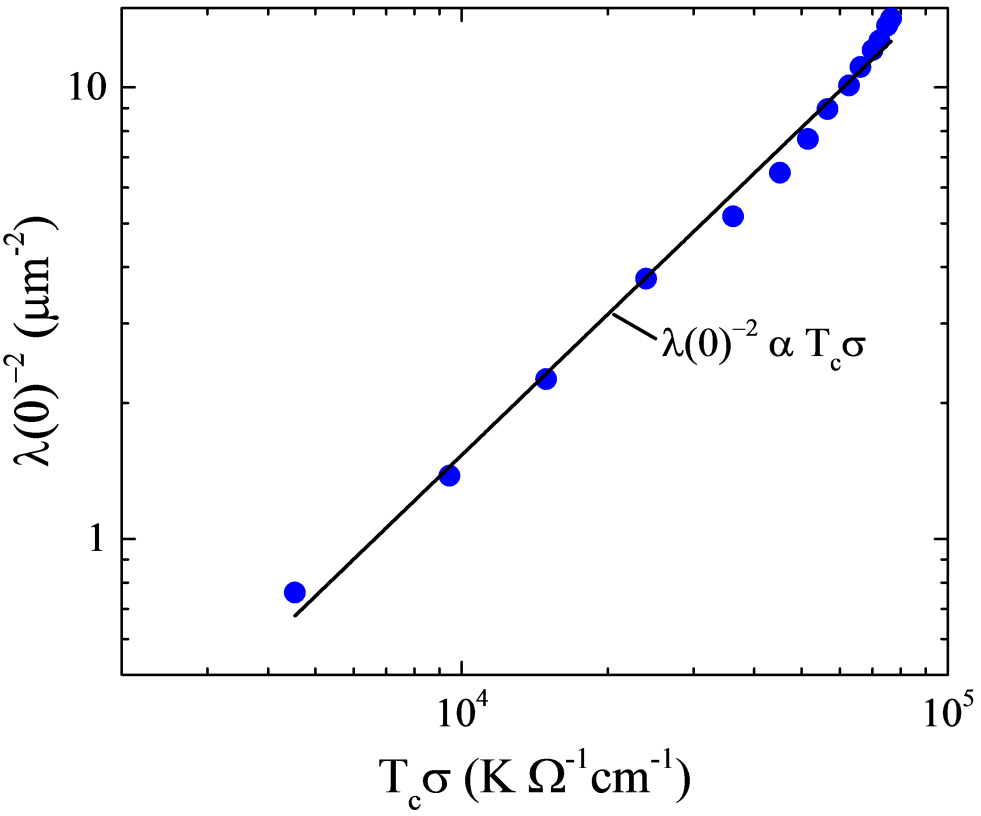

Figure 5.8: $\lambda(0)^{-2}$vs $T_c\sigma$ for a 3 unit cell LCO film. The properties of the film were systematically tuned using the ionic liquid and gate electrode setup pictured in Fig. 5.1. We see a linear relationship between $\lambda(0)^{-2}$and $T_c\sigma$ in agreement with the scaling relationship seen by Homes *et al.*

the electrons at energies less than the superconducting gap collapse into the superconducting state. If the superconducting gap is much smaller than the scattering rate, then the number of electrons that transition to the superconducting state, which is ρ_s, will be proportional to the product of the DC conductivity and the energy gap in the superconductor. If we take the transition temperature, T_c, as a proxy for the superconducting gap we see that the Homes scaling relationship of $\rho_s \propto T_c\sigma_{DC}$ follows from this simple argument. It is important to note that while the Homes data set is a compilation of many samples measured over the course

of many years, the data shown here is from a single sample continuously doped to cover a range of T_c values in a systematic and efficient manner. This points to the power of using ionic liquids in an electric double layer transistor configuration to systematically study the fundamental properties of superconducting samples.

It is important to examine to what extent the choices we made for defining T_c and σ effect the conclusion that the Homes scaling is a good model of our film. For the data plotted in Fig. 5.8 we define T_c as the temperature at which V_x is maximal and σ is taken using the value at 180 K. Both of these choices are clearly and unambiguously defined and produce a power of $x = 1.0$ using a linear fit of a Log Log plot of $\lambda(0)^{-2} \propto [\sigma T_c]^x$. If we instead define the conductivity using the value just above the transition but still use the maximal value of V_x to define T_c we find $x = 0.9$. If we adjust our definition of T_c to be the onset temperature of the $\lambda(T)^{-2}$ signal instead of the peak value we find $x = 1.5$ for either of the previous definitions of σ. The conclusion is that our result is particularly sensitive to our choice of how we define T_c. This is, in part, due to inhomogeneity in the film which leads to a broad superconducting transition.

5.4 Uemura Scaling

The initial motivation for exploring whether there is a fundamental relationship between T_c and $\lambda(0)^{-2}$ was derived from the empirical relationship proposed by Uemura *et al.*[44]. The data presented here does not follow the relationship proposed by Uemura of $T_c \propto \lambda(0)^{-2}$. This is actually readily seen by a more careful examination of Fig. 5.6. We see that the quantity $\lambda(0)^{-2}$, which is proportional to the superconducting electron density, increases linearly with the number of free carriers in the normal state. Simply, the number of superconducting electrons in

the superconducting state is proportional to the number of free holes in the normal state. This means that we could simply switch the x-axis of Fig. 5.6 from doping (carrier concentration) to $\lambda(0)^{-2}$ without affecting the shape of the T_c curve. This means the relationship between T_c and $\lambda(0)^{-2}$ will just be a remapping of the superconducting dome and therefore not a linear function as seen by Uemura in other, chemically doped high-T_c materials.

Figure 5.9 shows a plot of T_c vs $\lambda(0)^{-2}$, which would be a straight line with slope of 1 in the case of the scaling relationship established by Uemura. We see what looks like a sub linear power of $x = 0.7$ at the edge of the superconducting dome. Then a much smaller power $x < 0.2$ near the top of the dome. The power at the edge of the dome is similar to the 1/2 scaling seen by Zuev *et al.*[45] in thick $YBa_2Cu_3O_{6+x}$ films. This result could follow from the presence of a QCP at the edge of the dome where scaling arguments show that $\rho_s \propto \delta^{\nu(d+z-2)}$ and $T_c \propto \delta^{\nu z}$, which for the case of a 3d material reduce to $T_c \propto \rho_s^{0.5}$[42, 59, 60, 61]. If we fit the whole of our data we do get a power close to 0.5 but it looks like this is an average of two separate powers one near the edge of the dome and a different one near the top of the dome.

Alternatively we can take the above Homes scaling result and see that we should not expect a pure power law for our material. The Homes scaling shown in Fig. 5.8 establishes the result

$$T_c \sigma_{DC} \propto \rho_s \tag{5.4}$$

and from Fig. 5.6 we see that $\sigma \propto n_{2d}$ and $\rho_s \propto n - n_0$ where n_0 is the critical doping at the edge of the superconducting dome where superconductivity appears. The important fact here is that while both the conductivity and superconducting electron density are proportional to the 2D carrier concentration they go to zero at values shifted relative to each other. We can combine the previous two equations

to produce

$$\sigma \propto \rho_s + \rho_0 \tag{5.5}$$

where ρ_0 is a constant to account for the fact that conductivity is a power law centered about $n_{2d} = 0$ while the super-electron density is a power law centered about $n_{2d} = n_0$. Combining Eqn. 5.4 and Eqn. 5.5 we can produce an empirical relationship

$$T_c \propto \frac{\rho_s}{\rho_s + \rho_0}. \tag{5.6}$$

We see from this result that given the Homes scaling, a Drude model for the conductivity, and the empirical result of this thesis that $\rho_s \propto n - n_0$ we do not expect there to be a pure power law relationship between T_c and ρ_s.

Overall we have demonstrated a unique experimental setup where we can track resistance, doping, and penetration depth all in parallel for the same sample. This combination of measurements provide us with a direct means of probing the empirical scaling relationships established by Homes and Uemura. We observe that our results are in agreement with the scaling relationship of $\lambda^{-2} \propto \sigma T_c$ established by Homes and in disagreement with the scaling relationship of ${T_c}^2 \propto \lambda^{-2}$ established by Uemura. Finally, a primary result of this work is that the superconducting electron density is proportional to the normal state carrier concentration.

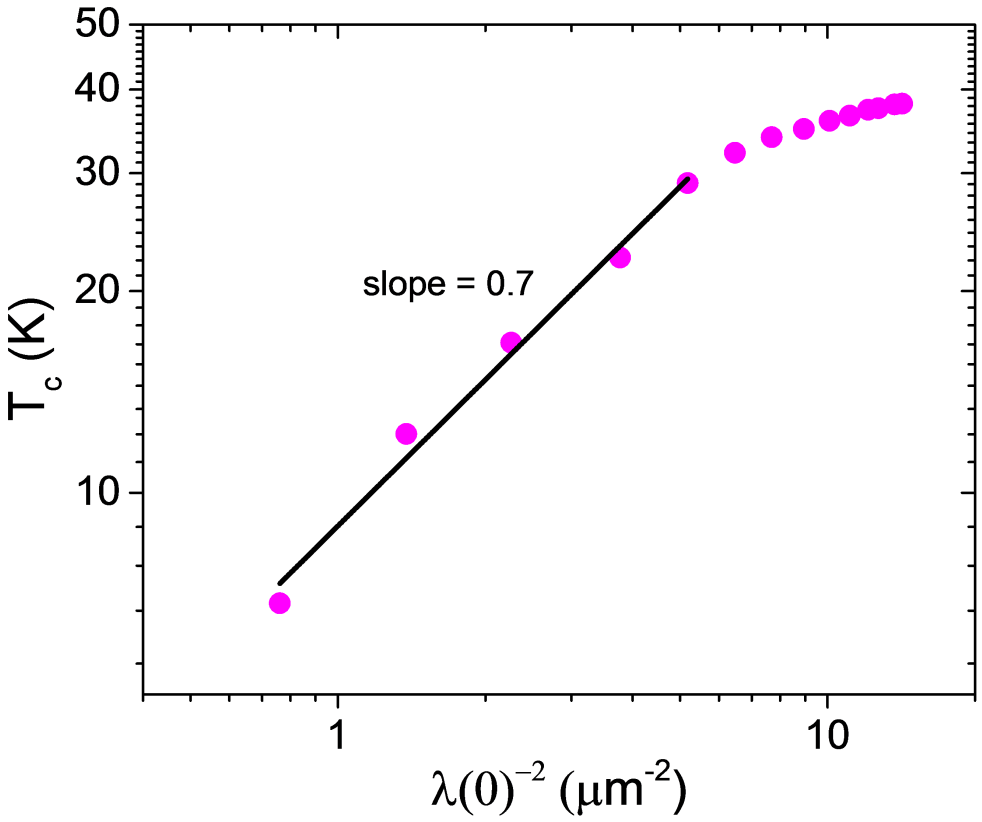

Figure 5.9: A plot of $\lambda(0)^{-2}$ vs T_c where the empirical Uemura relationship would show up as a straight line. If we only include the data at lower T_c values we have something approximately linear but there is no reason to break the data into that subset.

Chapter 6

Conclusions

The problem of finding superconducting materials that have higher and higher transition temperatures is of great technological interest. One of the primary hurdles to progress in this field is the nearly infinite material parameter space that needs to be explored. Ionic liquids offer the possibility of exploring this parameter space is a more efficient manner. Rather than needing to grow a whole series of samples at discrete dopings we have demonstrated the ability to continuously dope La_2CuO_{4+x} (LCO) superconducting thin films from optimal doping into the insulating state. While the initial promise of ionic liquids in recent years was of a tool that can cleanly adjust the doping in a purely electrostatic way, we see that for the combination of LCO and DEME-TFSI, the ionic liquid we chose for the studies presented in this work, there are electrochemical changes as well. While a purely electrostatic process has definite advantages in terms of reversibility, we find that a process that is closer to an *in situ* chemical doping mechanism is still a powerful and useful tool. In particular, we demonstrate that by explicitly measuring the doping of the film using the Hall Effect we can carefully track the nature of the changes effected by the ionic liquid.

In addition to being a more efficient means of exploring the doping parameter space, this tool allows us to systematically study how the resistance, transition temperature, doping, and penetration depth are all interconnected. We present an experimental setup that brings together ionic liquid doping, standard 4-wire transport measurements, and a two coil mutual inductance measurement of the penetration depth. This parallel combination of measurements is uniquely positioned to explore the empirical scaling relationships established by Homes[4, 5] and Uemura[44]. We find that our films fit the Homes scaling relationship and attribute this to the fact that scattering is strong in these films due to their ultra thin nature and effect of the roughness of the top and bottom surface. We find that Uemura relationship does not provide a good explanation of our measurements. In fact, a central result of our measurements is that the superconducting electron density is directly proportional to the normal state carrier concentration. A result of this proportionality is that instead of finding the Uemura relationship we see a simple remapping of the superconducting dome, which does not explicitly follow any power law.

Going forward, one of the primary challenges is to produce a more repeatable film growth process. As outlined in Sec. 2.1, the flux of the La and Cu sources during the MBE growth is only stable to about 10%. This means that the yield of high quality samples is low, also approximately 10%. There are many interesting experiments yet to be done involving high magnetic fields or continuations of the syncrotron studies mentioned in Sec. 3.2. The primary factor limiting these studies is the reproduction of high quality samples on demand.

Overall, we demonstrate the power of using ionic liquids to dope high temperature superconductors and efficiently explore the still not fully understood phase

diagram of these materials. Specifically, we find that the empirical scaling established by Homes is upheld in our measurements and we present a simple explanation for this result based of the fact that scattering is playing a significant role in these films. Ideally, this combination of more efficient searching through material space coupled to a firmer understanding of the fundamental driving forces of the superconducting state can lead to continued progress toward finding materials with higher still transition temperatures that could unlock many new technologies and applications.

References

[1] J. G. Bednorz and K. A. Müller. Possible high Tc superconductivity in the Ba-La-Cu-O system. *Zeitschrift für Physik B Condensed Matter*, 64(2):189–193, June 1986.

[2] Yoichi Kamihara, Takumi Watanabe, Masahiro Hirano, and Hideo Hosono. Iron-based layered superconductor La[$O_{1-x}F_x$]FeAs (x= 0.05-0.12) with Tc = 26 K. *Journal of the American Chemical Society*, 130(11):3296–3297, March 2008.

[3] John Sarro, Wai-Kwong Kwok, Ivan Bozovic, Igor Mazin, J. C. Seamus Davis, Leonardo Civale, and David Christen. Developing a Comprehensive and Predictive Theory of Superconductivity. *Report of the Basic Energy Sciences Workshop on Superconductivity*, 2006.

[4] C. C. Homes, S. V. Dordevic, M. Strongin, D. A. Bonn, Ruixing Liang, W. N. Hardy, Seiki Komiya, Yoichi Ando, G. Yu, N. Kaneko, X. Zhao, M. Greven, D. N. Basov, and T. Timusk. A universal scaling relation in high-temperature superconductors. *Nature*, 430(6999):539–41, July 2004.

[5] C. C. Homes. Scaling of the superfluid density in high-temperature superconductors. *Physica C: Superconductivity and its Applications*, 445-448(1-2):8–13, October 2006.

[6] P. G. Radaelli, J. D. Jorgensen, A. J. Schultz, B. A. Hunter, J. L. Wagner, F. C. Chou, and D. C. Johnston. Structure of the superconducting $La_2CuO_{4+\delta}$ phases ($\delta = 0.08, 0.12$) prepared by electrochemical oxidation. *Physical Review B*, 48(1):499–510, July 1993.

[7] S. Dzhumanov, O.K. Ganiev, and Sh.S. Djumanov. Normal-state conductivity of underdoped to overdoped cuprate superconductors: Pseudogap effects on the in-plane and c-axis charge transports. *Physica B: Condensed Matter*, 440:17–32, May 2014.

[8] C. H. Ahn. Electrostatic Modulation of Superconductivity in Ultrathin $GdBa_2Cu_3O_{7-x}$ Films, May 1999.

[9] C. H. Ahn, J.-M. Triscone, and J. Mannhart. Electric field effect in correlated oxide systems. *Nature*, 424(6952):1015–1018, August 2003.

[10] D. Matthey, N. Reyren, J.-M. Triscone, and T. Schneider. Electric-Field-Effect Modulation of the Transition Temperature, Mobile Carrier Density, and In-Plane Penetration Depth of $NdBa_2Cu_3O_{7-\delta}$ Thin Films. *Physical Review Letters*, 98(5):057002, January 2007.

[11] M. Salluzzo, A. Gambardella, G. M. De Luca, R. Di Capua, Z. Ristic, and R. Vaglio. Electronic phase separation near the superconductor-insulator transition of Nd $_{1+x}Ba_{2-x}Cu_3O_{7-\delta}$ thin films studied by an electric-field-induced doping effect. *Physical Review B*, 78(5):054524, August 2008.

[12] A. Rüfenacht, J.-P. Locquet, J. Fompeyrine, D. Caimi, and P. Martinoli. Electrostatic Modulation of the Superfluid Density in an Ultrathin $La_{2-x}Sr_xCuO_4$ Film. *Physical Review Letters*, 96(22):227002, June 2006.

[13] X. X. Xi, C. Doughty, A. Walkenhorst, C. Kwon, Q. Li, and T. Venkatesan. Effects of field-induced hole-density modulation on normal-state and superconducting transport in $YBa_2Cu_3O_{7-x}$. *Physical Review Letters*, 68(8):1240–1243, February 1992.

[14] Kevin A. Parendo, K. H. Sarwa B. Tan, and A. M. Goldman. Electrostatic and parallel-magnetic-field tuned two-dimensional superconductor-insulator transitions. *Physical Review B - Condensed Matter and Materials Physics*, 73(17):174527, May 2006.

[15] K. Ueno, S. Nakamura, H. Shimotani, A. Ohtomo, N. Kimura, T. Nojima, H. Aoki, Y. Iwasa, and M. Kawasaki. Electric-field-induced superconductivity in an insulator. *Nature materials*, 7(11):855–8, November 2008.

[16] Steven G. Haupt, David R. Riley, Christopher T. Jones, J N Zhao, and J T Mcdevitt. Reversible Modulation of Tc in Conductive Polymer High Temperature Superconductor Assemblies. *Journal of the American Chemical Society*, 115(3):1196–1198, February 1993.

[17] Stephen R. Peck, Larry S. Curtin, John T. McDevitt, Royce W. Murray, James P. Collman, William A. Little, T. Zetterer, H. M. Duan, C. Dong, and A. M. Hermann. Response of the double-layer capacitance of a high-temperature superconductor/fluid electrolyte interface to the onset of superconductivity. *Journal of the American Chemical Society*, 114(17):6771–6775, August 1992.

[18] A. T. Bollinger, G. Dubuis, J. Yoon, D. Pavuna, J. Misewich, and I. Božović. Superconductor-insulator transition in $La_{2-x}Sr_xCuO_4$ at the pair quantum resistance. *Nature*, 472(7344):458–60, April 2011.

[19] Xiang Leng, Javier Garcia-Barriocanal, Shameek Bose, Yeonbae Lee, and A. M. Goldman. Electrostatic Control of the Evolution from a Superconducting Phase to an Insulating Phase in Ultrathin $YBa_2Cu_3O_{7-x}$ Films. *Physical Review Letters*, 107(2):027001, July 2011.

[20] Xiang Leng, Javier Garcia-Barriocanal, Boyi Yang, Yeonbae Lee, J. Kinney, and A. M. Goldman. Indications of an Electronic Phase Transition in Two-Dimensional Superconducting $YBa_2Cu_3O_{7-x}$ Thin Films Induced by Electrostatic Doping. *Physical Review Letters*, 108(6):067004, February 2012.

[21] J. Garcia-Barriocanal, A. Kobrinskii, X. Leng, J. Kinney, B. Yang, S. Snyder, and A. Goldman. Electronically driven superconductor-insulator transition in electrostatically doped $La_2CuO_{4+\delta}$ thin films. *Physical Review B*, 87(2):024509, January 2013.

[22] S. W. Zeng, Z. Huang, W. M. Lv, N. N. Bao, K. Gopinadhan, L. K. Jian, T. S. Herng, Z. Q. Liu, Y. L. Zhao, C. J. Li, H. J. Harsan Ma, P. Yang, J. Ding, T. Venkatesan, and Ariando. Two-dimensional superconductor-insulator quantum phase transitions in an electron-doped cuprate. *Physical Review B*, 92(2):020503, July 2015.

[23] Trevor A. Petach, Menyoung Lee, Ryan C. Davis, Apurva Mehta, and David Goldhaber-Gordon. Mechanism for the large conductance modulation in electrolyte-gated thin gold films. *Physical Review B*, 90(8):081108(R), August 2014.

[24] Jaewoo Jeong, Nagaphani Aetukuri, Tanja Graf, Thomas D. Schladt, Mahesh G. Samant, and Stuart S. P. Parkin. Suppression of metal-insulator transition in VO_2 by electric field-induced oxygen vacancy formation. *Science (New York, N.Y.)*, 339(6126):1402–5, March 2013.

[25] Jaewoo Jeong, Nagaphani B. Aetukuri, Donata Passarello, Steven D. Conradson, Mahesh G. Samant, and Stuart S. P. Parkin. Giant reversible, facet-dependent, structural changes in a correlated-electron insulator induced by ionic liquid gating. *Proceedings of the National Academy of Sciences*, 112(4):1013–1018, January 2015.

[26] Andrew C. Lang, Jennifer D. Sloppy, Hessam Ghassemi, Robert C. Devlin, Rebecca J. Sichel-Tissot, Juan-Carlos Idrobo, Steven J. May, and Mitra L. Taheri. Atomic-Scale Characterization of Oxide Thin Films Gated by Ionic Liquid. *ACS Applied Materials and Interfaces*, 6(19):17018–17023, October 2014.

[27] Patrick Gallagher, Menyoung Lee, Trevor A. Petach, Sam W. Stanwyck, James R. Williams, Kenji Watanabe, Takashi Taniguchi, and David Goldhaber-Gordon. A high-mobility electronic system at an electrolyte-gated oxide surface. *Nat Commun*, 6:6437, March 2015.

[28] B. O. Wells, Y. S. Lee, M. A. Kastner, R. J. Christianson, F. C. Chou, R. J. Birgeneau, K. Yamada, Y. Endoh, and G. Shirane. Structural Phase Transitions and Incommensurate Spin Fluctuations in the La_2CuO_{4+y} System. NATO ASI Series, pages 349–370. Springer Netherlands, 1997.

[29] Michela Fratini, Nicola Poccia, Alessandro Ricci, Gaetano Campi, Manfred Burghammer, Gabriel Aeppli, and Antonio Bianconi. Scale-free structural

organization of oxygen interstitials in La_2CuO_{4+y}. *Nature*, 466(7308):841–844, August 2010.

[30] Leo J. van der Pauw. A method of measuring the resistivity and Hall coefficient on lamellae of arbitrary shape. *Philips Technical Review*, 20:220–224, 1958.

[31] Ronald Chwang, B.J. Smith, and C.R. Crowell. Contact size effects on the van der Pauw method for resistivity and Hall coefficient measurement, December 1974.

[32] James Annett, Nigel Goldenfeld, and S. R. Renn. Interpretation of the temperature dependence of the electromagnetic penetration depth in $YBa_2Cu_3O_{7-\delta}$. *Physical Review B*, 43(4):2778–2782, February 1991.

[33] A. Hebard and A. Fiory. Evidence for the Kosterlitz-Thouless Transition in Thin Superconducting Aluminum Films. *Physical Review Letters*, 44(4):291–294, January 1980.

[34] A. T. Fiory, A. F. Hebard, P. M. Mankiewich, and R. E. Howard. Penetration depths of high Tc films measured by two-coil mutual inductances. *Applied Physics Letters*, 52(25):2165, June 1988.

[35] B. Jeanneret, J. L. Gavilano, G. A. Racine, Ch Leemann, and P. Martinoli. Inductive conductance measurements in two-dimensional superconducting systems. *Applied Physics Letters*, 55(22):2336, November 1989.

[36] Zhong-Heng Lin. *Temperature dependence of the electromagnetic penetration depth of high temperature superconductors.* PhD thesis, University of Minnesota, United States – Minnesota, 1995.

[37] Z.-H. Lin, G. C. Spalding, A. M. Goldman, B. F. Bayman, and O. T. Valls. Temperature Dependence of the Penetration Depth of $YBa_2Cu_3O_{7-\delta}$ Films near T_c. *Europhysics Letters (EPL)*, 32(7):573–578, December 1995.

[38] John David Jackson. *Classical Electrodynamics*. John Wiley and Sons, Inc., third edition, 1999.

[39] A. Goyal, D. P. Norton, J. D. Budai, M. Paranthaman, E. D. Specht, D. M. Kroeger, D. K. Christen, Q. He, B. Saffian, F. A. List, D. F. Lee, P. M. Martin, C. E. Klabunde, E. Hartfield, and V. K. Sikka. High critical current density superconducting tapes by epitaxial deposition of $YBa_2Cu_3O_x$ thick films on biaxially textured metals. *Applied Physics Letters*, 69(12):1795–1797, September 1996.

[40] T. Startseva, T. Timusk, A. V. Puchkov, D. N. Basov, H. A. Mook, M. Okuya, T. Kimura, and K. Kishio. Temperature evolution of the pseudogap state in the infrared response of underdoped $La_{2-x}Sr_xCuO_4$. *Physical Review B*, 59(10):8, March 1998.

[41] G. Aeppli, E. J. Ansaldo, J. H. Brewer, R. J. Cava, R. F. Kiefl, S. R. Kreitzman, G. M. Luke, and D. R. Noakes. Magnetic penetration depth and flux-pinning effects in high-Tc superconductor $La_1.85Sr_0.15CuO$. *Physical Review B*, 35(13):7129–7132, May 1987.

[42] T. R. Lemberger, I. Hetel, A. Tsukada, M. Naito, and M. Randeria. Superconductor-to-metal quantum phase transition in overdoped $La_{2-x}Sr_xCuO_4$. *Physical Review B*, 83(14):140507, April 2011.

[43] C. C. Homes. Scaling of the superfluid density in high-temperature superconductors. *Physica C: Superconductivity and its Applications*, 445-448(1-2):8–13, October 2006.

[44] Y. Uemura, G. Luke, B. Sternlieb, J. Brewer, J. Carolan, W. Hardy, R. Kadono, J. Kempton, R. Kiefl, S. Kreitzman, P. Mulhern, T. Riseman, D. Williams, B. Yang, S. Uchida, H. Takagi, J. Gopalakrishnan, A. Sleight, M. Subramanian, C. Chien, M. Cieplak, Gang Xiao, V. Lee, B. Statt, C. Stronach, W. Kossler, and X. Yu. Universal Correlations between T_c and n_s/m^* (Carrier Density over Effective Mass) in High-T_c Cuprate Superconductors. *Physical Review Letters*, 62(19):2317–2320, May 1989.

[45] Yuri Zuev, Mun Seog Kim, and Thomas R. Lemberger. Correlation between Superfluid Density and TC of Underdoped $YBa_2Cu_3O_{6+x}$ Near the Superconductor-Insulator Transition. *Physical Review Letters*, 95(13):137002, September 2005.

[46] W. Hardy, D. Bonn, D. Morgan, Ruixing Liang, and Kuan Zhang. Precision measurements of the temperature dependence of λ in $YBa_2Cu_3O_{6.95}$: Strong evidence for nodes in the gap function, June 1993.

[47] M. Prohammer and J. P. Carbotte. London penetration depth of d -wave superconductors. *Physical Review B*, 43(7):5370–5374, March 1991.

[48] Peter J. Hirschfeld and Nigel Goldenfeld. Effect of strong scattering on the low-temperature penetration depth of a d -wave superconductor. *Physical Review B*, 48(6):4219–4222, August 1993.

[49] Kenichiro Hashimoto, Yuta Mizukami, Ryo Katsumata, Hiroaki Shishido, Minoru Yamashita, Hiroaki Ikeda, Yuji Matsuda, John A. Schlueter,

Jonathan D. Fletcher, Antony Carrington, Daniel Gnida, Dariusz Kaczorowski, and Takasada Shibauchi. Anomalous superfluid density in quantum critical superconductors. *Proceedings of the National Academy of Sciences of the United States of America*, 110(9):3293–7, February 2013.

[50] D. Einzel, P. J. Hirschfeld, F. Gross, B. S. Chandrasekhar, K. Andres, H. R. Ott, J. Beuers, Z. Fisk, and J. L. Smith. Magnetic Field Penetration Depth in the Heavy-Electron Superconductor UBe_{13}. *Physical Review Letters*, 56(23):2513–2516, June 1986.

[51] V. G. Kogan, R. Prozorov, and V. Mishra. London penetration depth and pair breaking. *Physical Review B - Condensed Matter and Materials Physics*, 88(22):224508, December 2013.

[52] Y. Imry, M. Strongin, and C. C. Homes. N_s-T_c correlations in granular superconductors. *Physical Review Letters*, 109(6):067003, August 2012.

[53] V. G. Kogan. Homes scaling and BCS. *Physical Review B*, 87(22):220507, June 2013.

[54] B. J. Taylor and M. B. Maple. Origin of critical temperature universal scaling relations in type-II superconductors. *Physical Review B*, 76(18):184512, November 2007.

[55] D. N. Basov and Andrey V. Chubukov. Manifesto for a higher Tc – lessons from pnictides and cuprates. *Nature Physics*, 7(4):272–276, April 2011.

[56] Makoto Hashimoto, Inna M. Vishik, Rui-Hua He, Thomas P. Devereaux, and Zhi-Xun Shen. Energy gaps in high-transition-temperature cuprate superconductors. *Nature Physics*, 10(7):483–495, July 2014.

[57] E. Razzoli, G. Drachuck, A. Keren, M. Radovic, N. C. Plumb, J. Chang, Y.-B. Huang, H. Ding, J. Mesot, and M. Shi. Evolution from a Nodeless Gap to $d_{x^2-y^2}$-Wave in Underdoped $La_{2-x}Sr_xCuO_4$. *Physical Review Letters*, 110(4):047004, January 2013.

[58] M. Hashimoto, T. Yoshida, K. Tanaka, A. Fujimori, D. H. Lu, Z. X. Shen, S. Wakimoto, M. Okusawa, and K. Yamada. Photoemission study of excess oxygen-doped $La_2CuO_{4.10}$. *Physica C: Superconductivity and its Applications*, 445-448(1-2):80–83, October 2006.

[59] Matthew P.A. Fisher. Theory of Superconductor-Insulator Transitions in Disordered Films. *Annals of the New York Academy of Sciences*, 581(1 Frontiers In):223–231, July 1990.

[60] Angela Kopp and Sudip Chakravarty. Criticality in correlated quantum matter. *Nature Physics*, 1(1):53–56, October 2005.

[61] Igor F. Herbut. Zero-Temperature d-Wave Superconducting Phase Transition. *Physical Review Letters*, 85(7):1532–1535, August 2000.